Advanced Composites and Hybrid Materials (2024) 7:93
https://doi.org/10.1007/s42114-024-00892-9

RESEARCH

Theoretically endured defect-engineered antimony selenide nanocrystals grafted within three-dimensional reduced graphene oxide hollow microspheres with large open cavities as polysulfide barrier for robust sulfur kinetics

Rakesh Saroha[1] · Dong Yun Shin[2] · Jae Seob Lee[1,3] · Sung Woo Cho[1] · Dong-Hee Lim[2] · Jung Sang Cho[1]

Received: 6 September 2023 / Revised: 4 December 2023 / Accepted: 17 April 2024
© The Author(s), under exclusive licence to Springer Nature Switzerland AG 2024

Abstract
Defect engineering techniques have gained significant attention worldwide as a promising strategy to amend the electronic and atomic arrangements of nanomaterials. By introducing defects such as dislocations or vacancies in polar materials, it is possible to create electrophilic adsorption sites that can effectively trap polysulfide species by lowering the energy transfer barrier for electrons. In this study, non-stoichiometric antimony selenide ($Sb_2Se_{2.2}$) nanocrystals embedded in a three-dimensional hollow microsphere composed of a reduced graphene oxide (rGO) matrix (H-$Sb_2Se_{2.2}$@rGO−600) were synthesized by precisely controlling the heating conditions. Density functional theory (DFT) calculations revealed that thermally induced anionic Se-defects caused atomic disorder in the crystal structure, altering the electronic structure and in turn enhancing the adsorption strength of polysulfide through improved electrophilic coupling interactions between $Sb^{\delta+} - S_x^{2-}$ and $Li^+ - Se^{\delta-}$. Lithium–sulfur (Li–S) batteries incorporating H-$Sb_2Se_{2.2}$@rGO−600-coated separator and a typical sulfur electrode (≈2.0 mg cm^{-2}) exhibited excellent high-rate capability, with a discharge rate of up to 4.0 C, and exceptional cycling stability. After 1300 continuous charge−discharge cycles at 4.0 C, the cell showed a capacity retention of 90.4%, with an average capacity decay rate of only 0.007% per cycle. The impressive performance was maintained under more demanding cell conditions, such as high effective S content (66%), high S loading (6.0 mg cm^{-2}), and a low electrolyte-to-sulfur ratio (4.3 µL mg^{-1}). The Li–S cell demonstrates excellent cycling stability (120 cycles at 0.1 C) and maintains feasible rate performance up to 0.3 C.

Keywords Lithium−sulfur batteries · Spray pyrolysis · Metalloid selenide · Defect engineering · Electrocatalytic interlayers

1 Introduction

The high theoretical discharge capacity (1675 mA h g^{-1}) and exceptional gravimetric energy density (2600 Wh kg^{-1}) have positioned lithium−sulfur (Li–S) batteries as a promising alternative to commercially available lithium-ion batteries [1–5]. However, the complex solid–liquid–solid phase separations involving sulfur (S), intermediate lithium polysulfide (LiPS) species, and final Li_2S product pose significant challenges in achieving satisfactory electrochemical performance in Li–S cells [6–10]. The presence of intermediate LiPS species has both advantageous and detrimental effects. While their fast electrocatalytic conversion is desirable for high sulfur utilization and improved battery performance, their shuttling between the cathode and anode under concentration gradient and electric field effects leads to severe cell degradation [11–15]. Therefore, efficient electrocatalytic

Rakesh Saroha, Dong Yun Shin, and Jae Seob Lee contributed equally to this work.

✉ Dong-Hee Lim
limkr@cbnu.ac.kr

✉ Jung Sang Cho
jscho@cbnu.ac.kr

[1] Department of Engineering Chemistry, Chungbuk National University, Chungbuk 361-763, Republic of Korea

[2] Department of Environmental Engineering, Chungbuk National University, Chungbuk 361-763, Republic of Korea

[3] Department of Materials Science and Engineering, Korea University, Anam-Dong, Seongbuk-Gu, Seoul 136-713, Republic of Korea

Published online: 17 May 2024

conversion of intermediate LiPS species is a key issue of focus in Li–S battery research [16–20].

In addition to localizing sulfur within the porous hosts, utilizing functional separators or interlayers in which the coated part faced towards the sulfur side is another promising strategy to restrict the polysulfide migration within the cathodic domain. The interlayers acted as a "polysulfide barrier" and generally consisted of three parts: a conductive matrix that supports fast redox kinetics; a porous framework for efficient electrolyte infiltration; and finally, a polar material for providing abundant chemisorption sites for effective polysulfide anchoring. Numerous transition metal compounds (TMCs) have been explored for confining S and regulating LiPS species due to their strong chemical interactions with the polysulfide species [21, 22]. TMCs mainly constitute transition metal oxides (TMOs), transition metal nitrides (TMNs), transition metal sulfides (TMSs), transition metal carbides (TMCs), transition metal selenides (TMSes), and transition metal phosphides (TMPs) [23–28]. In particular, TMSes have emerged as promising electrocatalytic materials owing to their unique structure (sandwiched configuration in the form of Y–M–Y, where M is a transition metal, and Y is Se). TMSes are also characterized by Van der Waals forces, low cost, high electrical conductivity, narrow-bandgap semiconducting properties, strong spin-orbit coupling, and superior electrocatalytic activity towards LiPS [29]. The strong interaction between TMSes and LiPS reduces the reaction energy barrier for intermediate polysulfides, leading to a shortened nucleation path for Li_2S [30]. Additionally, the presence of lithophilic as well as sulfiphilic sites in TMSes simultaneously minimizes Li dendrite formation or growth by enabling uniform Li^+ deposition along with the efficient trapping of LiPS, preventing active material loss [21]. However, issues such as poor ion diffusion and parasitic interface/surface chemical reactions are associated with TMSes [27]. Additionally, chemisorption sites are only available on the edge planes of TMSes rather than the basal planes due to their limited coordinated active sites and low Gibbs free energy [31, 32].

Defect engineering techniques have garnered significant attention as a paramount strategy for modifying the electronic and atomic arrangements of nanomaterials. Introducing defects, such as dislocations or vacancies, in polar materials creates numerous electrophilic adsorption sites capable of trapping LiPS species by reducing the energy transfer barrier for electrons [6]. In addition, defects also cause variations in surface energy among different crystal planes, resulting in different chemical trapping and catalytic activation abilities. This is primarily due to the interaction or transfer of frontier orbital electrons from polysulfide species to empty or electron-vacant sites in polar nanomaterials [33]. However, research solely focused on enhancing the performance of Li–S cells based on selenium (Se) vacancies or deficiencies is still in the early stages. Furthermore, studies specifically investigating the defect-induced electrocatalytic ability of particular crystal planes are scarce. Herein, we present a detailed comprehensive analysis based on computational (density functional theory (DFT)) as well as experimental analysis demonstrating how the introduction of Se-dislocations or Se-defects enhances the LiPS adsorption efficiency of particular crystal planes, along with optimal microstructure design strategy for Li-S batteries.

In this study, we prepared a non-stoichiometric antimony selenide phase by accurately controlling the heating conditions and utilizing it as a coating interlayer at the cathode side to enhance the electrochemical performance of Li–S cells. Notably, stoichiometric antimony selenide (Sb_2Se_3) exhibits P-type semiconductivity with a narrow bandgap of approximately 1.1 eV [34, 35]. Additionally, the absence of dangling bonds at the grain boundaries in Sb_2Se_3 allows for heterostructure formation, which facilitates excellent Li-ion transmission and storage characteristics due to irregular charge spreading [34, 36]. Moreover, Se-defects or vacancies can be easily introduced and controlled in Sb_2Se_3 owing to the facile evaporation of Se. We employed a scalable spray pyrolysis process to initially synthesize hollow three-dimensional (3D) microspheres comprising antimony/antimony oxide (Sb/Sb_2O_3) nanocrystals embedded in a reduced graphene oxide (rGO) framework and then carried out a selenization process in a reducing atmosphere (5% H_2/Ar). The selenization temperature was optimized by synthesizing a series of samples at different temperatures. The final optimized powder was abbreviated as "H-$Sb_2Se_{2.2}$@rGO−600" microspheres. At the optimized temperature (600 °C), thermally induced Se-vacancies or dislocations were introduced to eventually form a non-stoichiometric antimony selenide ($Sb_2Se_{2.2}$) phase. Additionally, the self-supporting rGO framework provided multiple conductive pathways for fast electron transfer during the electrochemical process, while stabilizing the 3D hollow nanostructure. The hollow structure was formed due to the decomposition of the organic units in tartaric acid ($C_4H_6O_6$), whereas the cavities were introduced using a polystyrene (PS)-nanobead-based suspension ($\phi = 200$ nm). The hollow structure with open cavities facilitated smooth diffusion of charged species by shortening the effective charge diffusion length, minimizing electrolyte volume consumption, and accommodating volume variations during the lithiation/delithiation processes, leading to improved performance.

Based on the aforementioned nanostructural advantages, Li–S cells incorporating the H-$Sb_2Se_{2.2}$@rGO−600-modified separator exhibited remarkable electrochemical performance. The Li–S cells with nominal S loading (2.0 mg cm^{-2}) and an effective S content of 60.4% demonstrated a high-rate capability up to 4.0 C and significant cycling stability at 4.0 C (until 1300 cycles). Even under more challenging

battery parameters (effective S content of 66%, S loading of 6.0 mg cm^{-2}, and a low electrolyte-to-sulfur ratio of 4.3 µL mg^{-1}), Li–S cells utilizing the H-$Sb_2Se_{2.2}$@rGO−600-modified separator exhibited excellent rate (up to 0.3 C) and cycling performances (120 cycles at 0.1 C). Therefore, we anticipate that the structural benefits induced by defects will pioneer new insights in pursuit of more durable sulfur redox kinetics in various metal–sulfur batteries and other applications [37, 38].

2 Results and discussion

2.1 Nanostructure optimization for durable Li–S batteries

A thorough analysis of the synthesized microspheres was carried out to investigate their morphological and crystal structure characteristics at each step of the synthesis process. Fig. S1 presents the FE-SEM micrographs, XRD pattern, and Raman spectrum of the as-sprayed microspheres. The FE-SEM micrograph in Fig. S1a demonstrates the formation of non-aggregated, uniformly dispersed microspheres. Furthermore, the microspheres exhibit a nearly even size distribution with an average diameter of ≈1.5 µm. Upon closer inspection of Fig. S1b, a slight convex shape and surface roughness are observed, indicating effective confinement of the constituents within the prepared microspheres. Besides, the decomposition of PS nanobeads resulted in the formation of hollow cavities. However, in some regions, the PVP-derived carbonaceous species covers the outer surface of the microspheres, thus not exposing the cavities well. The XRD pattern (Fig. S1c) displays well-resolved diffraction peaks with biphasic characteristics indexed to the Sb and Sb_2O_3 phases. Additionally, a distinct hump at 2θ = 22° confirms the presence of rGO in the microspheres. Raman spectroscopy was employed to examine the crystalline properties of carbonaceous species. The spectrum (Fig. S1d) reveals distinct D- and G-band signatures located at 1351 and 1575 cm^{-1}, respectively. The relative intensity ratio (*RIR*) of these two bands, denoted as I_D/I_G, provides a direct measure of the carbonaceous species crystallinity [39]. The obtained *RIR* value of 0.8 indicates the highly crystalline nature of the rGO framework constituting the microspheres. Furthermore, the two low-intensity peaks observed at the lower-wavenumber side are attributed to Sb–O bond stretching [40]. Overall, the results indicate the formation of biphasic nanostructures comprising well-confined Sb and Sb_2O_3 nanocrystals within a crystalline carbon framework derived from rGO.

To optimize the nanostructure in terms of morphology and crystal structure, the as-sprayed microspheres were subjected to a selenization process in a reducing atmosphere (5% H_2/Ar) at varying temperatures ranging from 350 to 700 °C. The resulting morphological and phase variations in the powders as a function of selenization temperature were examined, as shown in Fig. 1. Surprisingly, increasing the temperature from 350 to 700 °C led to subtle changes in microsphere size, while the overall morphological changes were not conspicuous, as observed in the FE-SEM micrographs (Fig. 1a–f). All selenized powders exhibited the formation of hollow microspheres with large cavities or voids, attributed to the thermal degradation of tartaric acid and PS nanobeads (ϕ = 200 nm). However, the XRD patterns (Fig. 1g) revealed significant alterations in the crystal environment as the temperature increased. The XRD peaks of all the powders indexed well with the standard JCPDS file for Sb_2Se_3 (orthorhombic crystal lattice; *Pbnm* space group). Notably, the highest-intensity peak at 2θ = 31.1° corresponds to the (221) diffraction plane of the crystal lattice. The selenized powder at 350 °C exhibited a well-matched diffraction peak, indicating the presence of the stoichiometric Sb_2Se_3 form. However, some additional peaks related to the pure Sb phase (marked with an asterisk) were also observed. Interestingly, as the selenization temperature increased from 400 to 600 °C, the intensity of the (221) plane faded continuously, while the intensity of the (120) plane reached a maximum at 500 °C and then decreased at 600 °C. This intensity transition from the (221) crystal plane to the (120) plane suggests significant changes in the atomic arrangement within the nanostructure associated with the specific planes. However, at 700 °C, only a broad hump at 2θ = 22° was observed, indicating the absence of sharp diffraction peaks corresponding to the selenide phase, leaving behind carbonaceous products only. This is due to the complete decomposition of the antimony selenide phase (melting point of ≈610 °C) at 700 °C. To gain deeper insight into the atomic environment variation of the selenized microspheres, elemental composition analysis was conducted using inductively coupled plasma optical emission spectrometry (ICP-OES) of samples prepared at different temperatures. The results (Table S1) revealed that lower selenization temperatures maintained a near stoichiometric composition. However, a selenization temperature of 500 °C resulted in a slightly non-stoichiometric atomic composition of Sb and Se. Notably, the highest degree of non-stoichiometry was observed at a selenization temperature of 600 °C, which yielded an experimental composition of $Sb_2Se_{2.2}$. This non-stoichiometric proportion at higher temperatures arose from the removal of Se from the crystal structure, leading to thermally induced Se-vacancies or Se-deficiencies. It is surmised that Se-vacancies introduce a high degree of atomic disorder and create coordinatively unsaturated catalytic sites, consequently enhancing the electrophilic coupling interactions between the polar material and polysulfide species. Electron probe microanalysis (EPMA) revealed the elemental mapping distribution in H-$Sb_2Se_{2.2}$@rGO−600 (Fig. S2), in which C, Se, and Sb

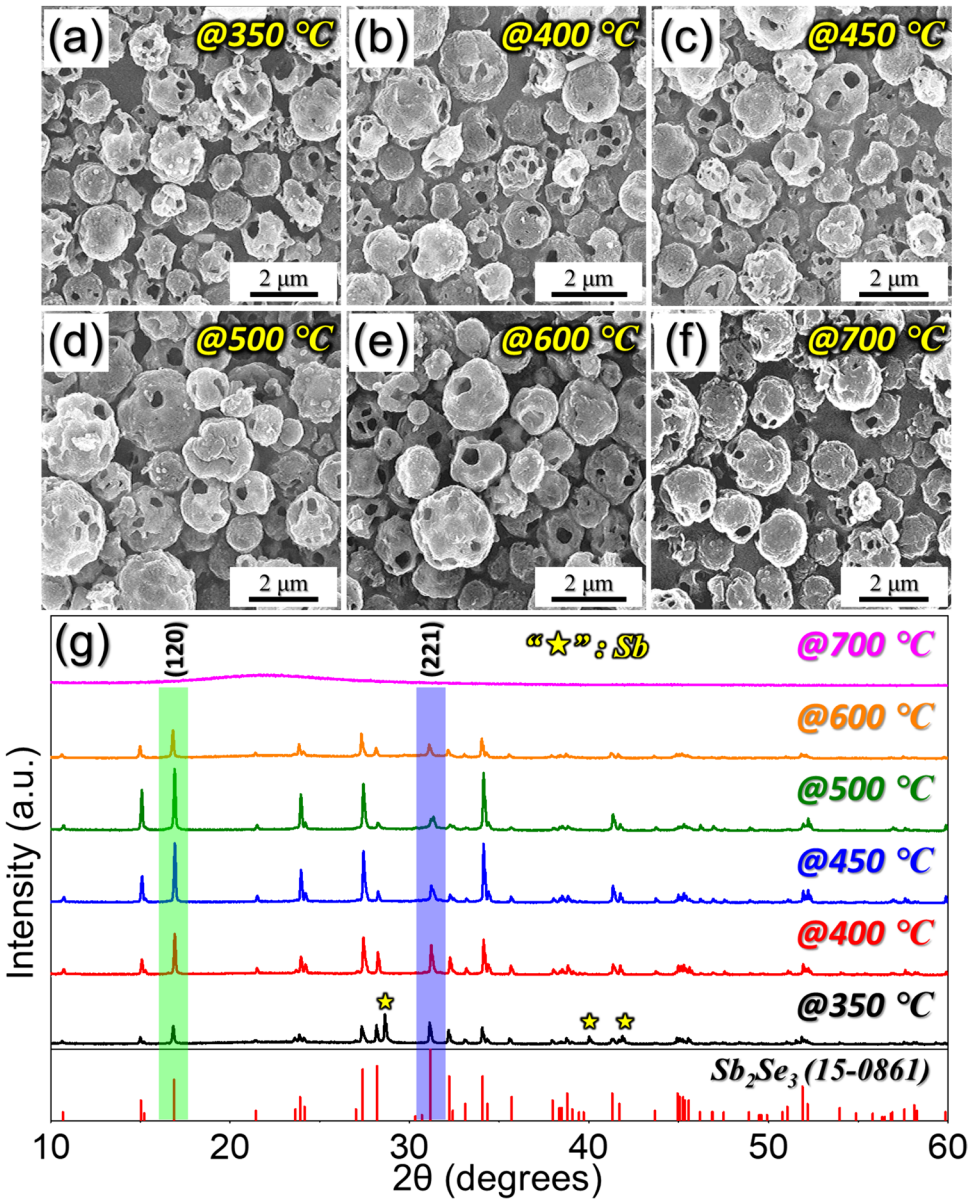

Fig. 1 Morphological and crystal structure characterizations of the as-sprayed composite microspheres after selenization at various temperatures for 3 h in a reducing atmosphere (5% H_2/Ar): **a**–**f** FE-SEM micrographs, and **g** XRD pattern variations as a function of selenization temperature

were uniformly distributed within the nanostructure. Consequently, increasing the selenization temperature offers the possibility of obtaining a non-stoichiometric form of antimony selenide, which could contribute to improving electrochemical performance due to the abundance of unsaturated electrocatalytic sites in the form of Se-vacancies.

2.2 Computational insights into the polysulfide adsorption capability of the Se-defect phase

Before conducting preliminary electrochemical tests, a computational investigation was undertaken to assess the potential use of the Se-deficient or non-stoichiometric form of Sb_2Se_3 towards the chemical adsorption of LiPS species. Initially, we designed the geometry of bulk stoichiometric Sb_2Se_3 (Fig. S3a and b) and subsequently optimized the (120) and (221) surfaces (Fig. S3c and d). The optimized bulk Sb_2Se_3 structure exhibited lattice parameters of approximately $a = 11.43$ Å, $b = 11.71$ Å, and $c = 4.02$ Å, which are consistent with previous studies [41]. Additionally, the geometries of different gas-phase sulfur-containing molecules, including S_8, Li_2S_6, and Li_2S_4 (Fig. S3e), were also optimized along with the corresponding bond lengths and bond angles (Table S2), which matches well with previous studies [42]. To evaluate the efficiency of the Sb_2Se_3 (120) and (221) surfaces for the LSBs, the adsorption energies of different key molecules involved in the shuttle reaction, including S_8, Li_2S_6, and Li_2S_4, were calculated. Notably, Li_2S_6 demonstrated the highest solubility, whereas Li_2S_4 was identified as a crucial intermediate determining the

LSB efficiency [43, 44]. Moreover, a more negative adsorption energy indicates a lower solubility of LiPS in the electrolyte. The adsorption energy calculation considered sites where Li- or S-atoms, as adsorbates, could react with Sb- or Se-atoms on the surfaces (Li–Sb, Li–Se, S–Sb, and S–Se adsorption models). The results indicated stable adsorption of S_8, Li_2S_6, and Li_2S_4 on the bulk stoichiometric Sb_2Se_3 (120) and (221) surfaces, where the Li of LiPSs was strongly adsorbed to the Se sites on the Sb_2Se_3 surfaces. The most stable adsorption energies of S_8, Li_2S_6, and Li_2S_4 on the bulk Sb_2Se_3 (120) surface were −1.07, −1.54, and −1.59 eV, respectively, while on the bulk Sb_2Se_3 (221) surface, they were −0.95, −2.08, and −1.80 eV, respectively (Fig. 2a–f). The adsorption energies of S_8, Li_2S_6, and Li_2S_4 on the pristine and defective Sb_2Se_3 (120) and (221) surfaces are shown in Tables S3 and S4. These findings clearly signify that for bulk stoichiometric Sb_2Se_3, the (221) surface is highly favorable for polysulfide adsorption compared to the (120) surface. Furthermore, defective Sb_2Se_3 (120) and (221) surfaces were also designed by removing the Se-atoms, which have a lower boiling point than Sb-atoms. Figure 2g and h illustrate Li_2S_6 adsorption configurations on the bulk Sb_2Se_3 (120) surface and non-stoichiometric or defective Sb_2Se_{3-x} (120) surface, respectively, featuring two Se-atom vacancies.

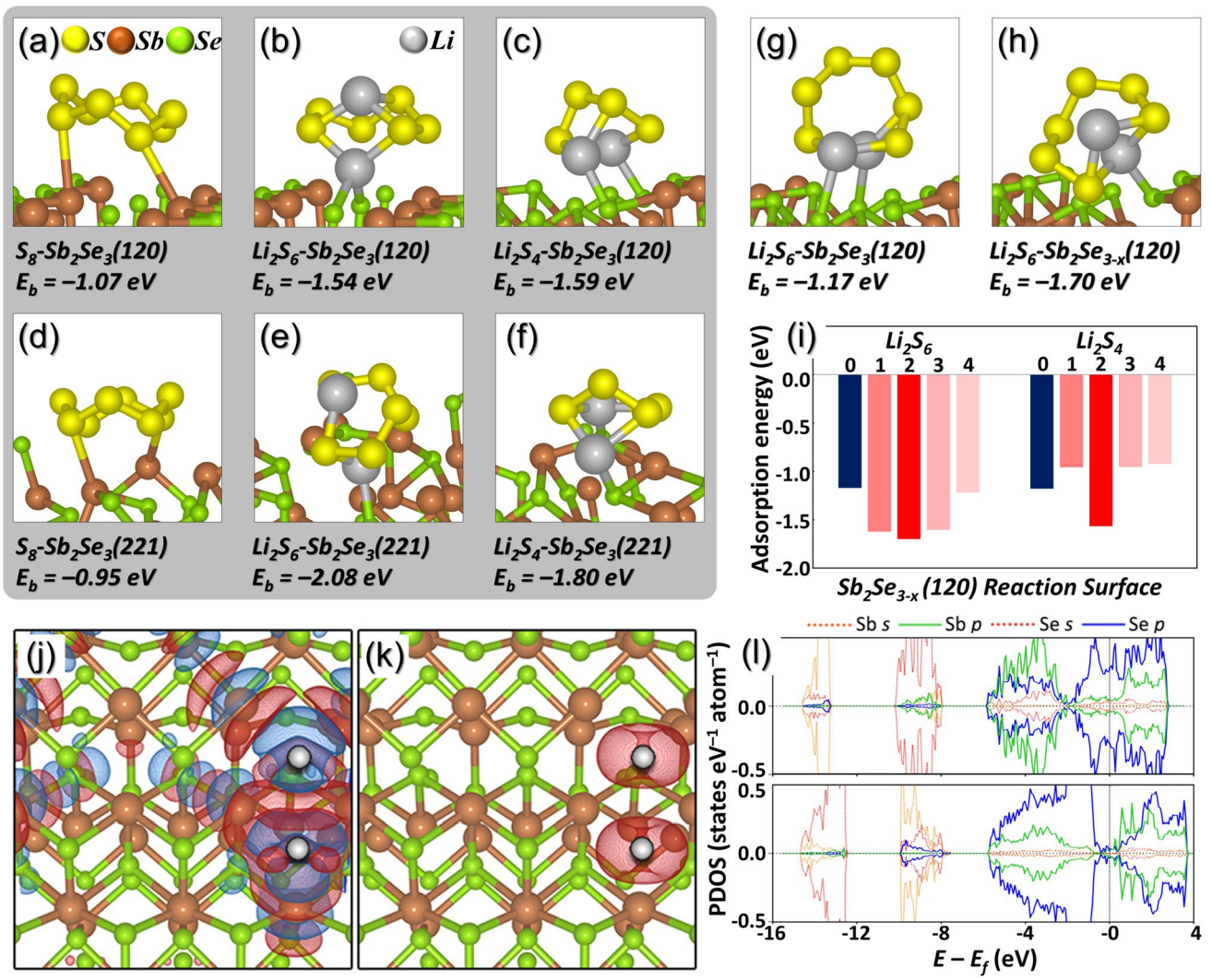

Fig. 2 The most stable adsorption configurations of **a** S_8, **b** Li_2S_6, and **c** Li_2S_4 on bulk stoichiometric Sb_2Se_3 (120) surface and **d** S_8, **e** Li_2S_4, and **f** Li_2S_6 on Sb_2Se_3 (221) surface; **g** Li_2S_6 adsorption configurations on bulk stoichiometric Sb_2Se_3 (120) surface and **h** defective Sb_2Se_3 (120) surface with two Se-atom vacancy sites; **i** adsorption energy dependence on the number of vacancy sites for Li_2S_6 and Li_2S_4 on Sb_2Se_{3-x} (120) and (221) surfaces; **j** charge density difference (CDD) and **k** spin density of Sb_2Se_3 (120) surface upon two Se-atom vacancy sites (red and blue colors in **j** represent charge accumulation and depletion upon Se-atom desorption, respectively, whereas red color in **k** is a positive spin density); and **l** projected density of states (PDOS) of bulk stoichiometric (above) and defective (two Se-atoms) Sb_2Se_{3-x} (120) surface (below). Silver, yellow, brown, green, and white spheres represent Li, S, Sb, Se-atoms, and Se-atom vacancy site, respectively

It was observed that Li_2S_6 interacted more strongly with atoms on the defective (120) surface ($E_b = -1.70$ eV) compared to the pristine Sb_2Se_3 (120) surface ($E_b = -1.17$ eV). It should be noted that the adsorption strength on the Sb_2Se_3 (120) surface depended on the number of Se-atom vacancies. Moreover, the adsorption strength of LiPS varied with the number of defective sites (Fig. 2i; "0" represents pristine surface whereas "1–4" represent a number of defects), indicating that an appropriate number of Se-atom defective sites are necessary to enhance the adsorption strength of LiPS. Electronic structure analyses demonstrated that the enhanced adsorption strength of LiPS resulted from the formation of dangling bonds by removing Se-atoms at the defective site. Figure 2j displays the charge density difference (CDD) of the defective Sb_2Se_{3-x} (120) surface, where Li_2S_6 exhibited the most stable adsorption, indicating actively interacting electrons at the Se-atom defect site. Additionally, Fig. 2k depicts the positive spin density at the defective site. Importantly, the spin density relies on the magnetization induced by the electron spin, where a higher positive spin density corresponds to stronger adsorption [45, 46]. The Sb_2Se_3 (120) surface used in this study has a flat arrangement of atoms, whereas the atoms on the Sb_2Se_3 (221) surface exhibit a stepped arrangement. Moreover, the stepped arrangement can be varied referring to the surface atom termination and thus is an important factor that can affect the adsorption strength [47]. To confirm this effect, the Sb_2Se_3 (221) surface (Sb termination) was designed by removing the Se-atoms exposed on the top of the Sb_2Se_3 (221) surface (Se termination), which was used in the above adsorption energy calculations. Further, adsorption energy was calculated on the Sb_2Se_3 (221) surface (Sb termination), in which S-atoms of the Li_2S_6 adsorbate were adsorbed on Sb-atoms. As a result, it was confirmed that Li_2S_6 exhibited weaker adsorption on the Sb-terminated Sb_2Se_3 (221) surface (−0.30 eV) than on the Se-terminated Sb_2Se_3 (221) surface (−0.42 eV), indicating Se-terminated surfaces exhibited more stable adsorption energies. Figure 2l illustrates the projected density of states (PDOS) when Li_2S_6 is adsorbed on bulk and defective Sb_2Se_3 (120) surfaces. On the defective surface, the electronic state of Se (4*p* orbitals) was located near the Fermi level (below panel). Particularly, the electronic state of Sb (5*s* and 5*p* orbitals) shifted closer to the Fermi level, implying that unlike the bulk surface, Sb-atoms can contribute to stable adsorption on the defective surface. Moreover, it has been reported that the closer the *p*-band center is to the Fermi level, the stronger the adsorption [48]. Notably, the *p*-band is an energy level value of the centroid in *p*-orbitals. In other words, electron donation is promoted, and a high strong adsorption strength is induced when more electrons are located near the fermi level. The *p*-band centers (below the Fermi level) of the Sb- and Se-atoms, where Li_2S_6 is adsorbed on the defective Sb_2Se_3 (120) surface, were −3.83 eV and −2.79 eV, respectively. These energies are closer to the Fermi level than the *p*-band center of the pristine Sb_2Se_3 (120) surface (Sb, −3.93 eV; Se, −2.82 eV). Overall, the computational calculations indicate that the nanostructure with thermally induced Se-vacancies exhibits enhanced adsorption of the polysulfide species due to more active bonding sites. These findings demonstrate the improved sulfur redox kinetics, which ultimately enhances electrochemical performance.

Taking advantage of the high degree of disorder in the atomic configuration of the H-$Sb_2Se_{2.2}$@rGO−600 microspheres, we performed preliminary rate capability tests from 0.05 to 4.0 C to better understand the effect of thermally induced Se-vacancies and validate the computational results. The prepared microspheres were utilized as electrocatalytic interlayers facing towards the cathode, and the rate capability results are summarized in Fig. 3. The microspheres obtained after selenization at 350 °C exhibited low discharge capacities (Fig. 3a), even at low C-rates of 0.05 and 0.1 C. Besides, at high C-rates of 2.0 C, the charge–discharge

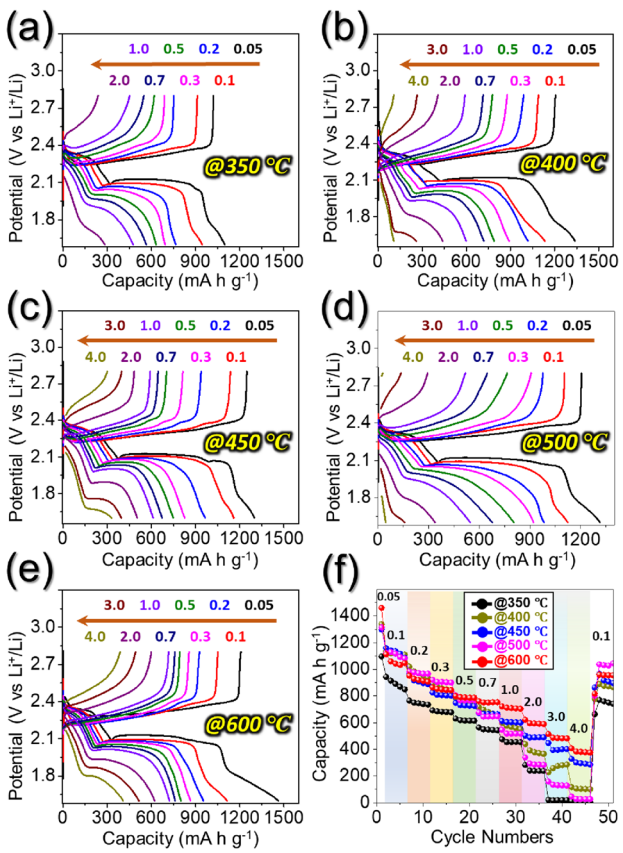

Fig. 3 Galvanostatic charge–discharge (GCD) voltage profiles and rate capability result at various current rates from 0.05 to 4.0 C for different powders prepared at various selenization temperatures: **a** 350 °C, **b** 400 °C, **c** 450 °C, **d** 500 °C, **e** 600 °C, and **f** rate performance of the prepared nanostructures

voltage plateaus were less pronounced. Furthermore, at C-rates higher than 2.0 C, no voltage profiles were obtained, implying insignificant discharge capacity values (Fig. 3f) owing to the inferior sulfur redox processes within the cell. Similar rate capabilities were obtained for microspheres prepared after selenization at 400 °C (Fig. 3b and f), although a slight improvement was noticeable. Furthermore, when the selenization temperature was further increased to 450 °C (Fig. 3c and f), the capacities considerably improved, particularly at high C-rates of 2.0, 3.0, and 4.0 C, with clear charge–discharge voltage plateaus. However, significant polarization at high C-rates was also evident, suggesting sluggish reaction kinetics. Similar results were observed for microspheres prepared at a selenization of 500 °C (Fig. 3d and f). However, at a selenization temperature of 600 °C, typical charge–discharge voltage plateaus were observed not only at low-C-rates but also at high C-rates (Fig. 3e). Besides, minimal voltage hysteresis was observed, indicating kinetically favored redox processes inside the Li–S cell. This resulted in high discharge capacity values at all C-rates, as shown in Fig. 3f. These preliminary results indicate that the atomic disorder in the crystal lattice of Sb_2Se_3 owing to Se-vacancies improved the chemical interaction between the polysulfide species and the active sites, consequently enhancing the utilization percentage of the active material. However, before performing a comprehensive electrochemical analysis, we inclusively examined the morphology, crystal structure, and crystallinity of the prepared nanostructure, as discussed below.

2.3 Physical analysis of the prepared nanostructure

As depicted in Fig. S1, the as-sprayed composite microspheres were subjected to a selenization process at 600 °C in a reducing atmosphere to obtain Se-deficient phase, namely H-$Sb_2Se_{2.2}$@rGO−600. The FE-SEM micrographs in Fig. 4a reveal that the spherical-type morphology was maintained even after selenization, with an average diameter of ≈1.5 µm. Besides, the microspheres contain hollow cavities (Fig. 4b), primarily due to the emission of large amounts of gases formed as a result of the thermal decomposition of tartaric acid and organic materials. Furthermore, these cavities were formed all over the microsphere owing to the complete thermal breakdown of the PS nanobeads ($\phi = 200$ nm). The hollow structure with large open cavities offers smooth diffusion of charged species by shortening the effective charge diffusion length, lowering the overall electrolyte volume consumption inside the cell, and channelizing the severe volume variations during the lithiation/delithiation processes. The TEM image in Fig. 4c is in accordance with the FE-SEM results, confirming the synthesis of hollow microspheres with open cavities surrounded by a 43-nm-thick shell of the carbonaceous species primarily formed by rGO. The presence of rGO nanosheets is apparent in the high-magnification TEM image (Fig. 4d). Notably, besides stabilizing the 3D hollow nanostructure, the self-supporting rGO framework provides numerous conductive pathways for fast electron transfer during the electrochemical process. Furthermore, well-confined Se-deficient nanocrystals are also evident. The high-resolution TEM (HR-TEM) image in Figs. 4e and S4 also reveals well-resolved lattice fringes separated by a distance of 0.29 nm, which correspond to the (211) diffraction plane of $Sb_2Se_{2.2}$ nanocrystals surrounded by the rGO framework. It should be noted that both the bulk and Se-deficient antimony selenide phases have the same crystal structure with identical 2θ peak positions, as evident from the XRD pattern in Fig. 1g. The crystallite size of the Se-deficient $Sb_2Se_{2.2}$ nanocrystals was determined to be ≈41 nm by applying the Scherrer equation to the (221) diffraction peak in Fig. 1g. Furthermore, the HR-TEM image in Fig. S4 was investigated by fast Fourier transform (FFT) pattern, which indicates recognizable atomic point Se-defects, as highlighted by yellow circles in Fig. 4f. Furthermore, disordered lattice and edge dislocations are also observed in the inverse FFT (IFFT) image (Fig. 4g, purple frame) alongside the perfect crystalline structure (red frame). The expanded interplanar spacing for disordered lattice (Fig. 4h, purple frame) compared to the perfect crystalline structure (Fig. 4h, red frame) clearly validated the defective nature of the H-$Sb_2Se_{2.2}$@rGO–600 sample. These lattice defect sites behave as trapping centers for charge species and enhance their electron transfer efficacy. The selected-area electron diffraction (SAED) pattern shown in Fig. 4i reveals well-distinguished diffraction rings corresponding to bulk stoichiometric Sb_2Se_3. In addition, a diffraction ring corresponding to the rGO-derived carbonaceous species, i.e., (002), is also evident. The elemental dot mapping images in Fig. 4j reveal the formation of hollow microspheres with large open cavities along with the uniform dispersion of Sb, Se, C, and N elements. The existence of N in the prepared nanostructure is due to the presence of the N-vinylpyrrolidone monomer in polyvinylpyrrolidone (PVP). Overall, the morphological and crystal structure analyses confirm the formation of 3D hollow microspheres with large open cavities enveloped within a self-supported rGO framework along with well-trapped, thermally derived Se-deficient antimony selenide nanocrystals within the structure.

Based on the above discussion, we summarize the detailed formation mechanism of H-$Sb_2Se_{2.2}$@rGO−600 microspheres in Scheme 1. Scheme 1a-① implies that the aqueous droplets formed by the atomic nebulizer consist of a uniformly distributed Sb tartrate complex, GO, PVP as a carbon source, and a PS suspension ($\phi = 200$ nm). Subsequently, the droplets passed through a vertically placed quartz tube that had been preheated to 500 °C, with flowing N_2 as the carrier gas. This process resulted in the

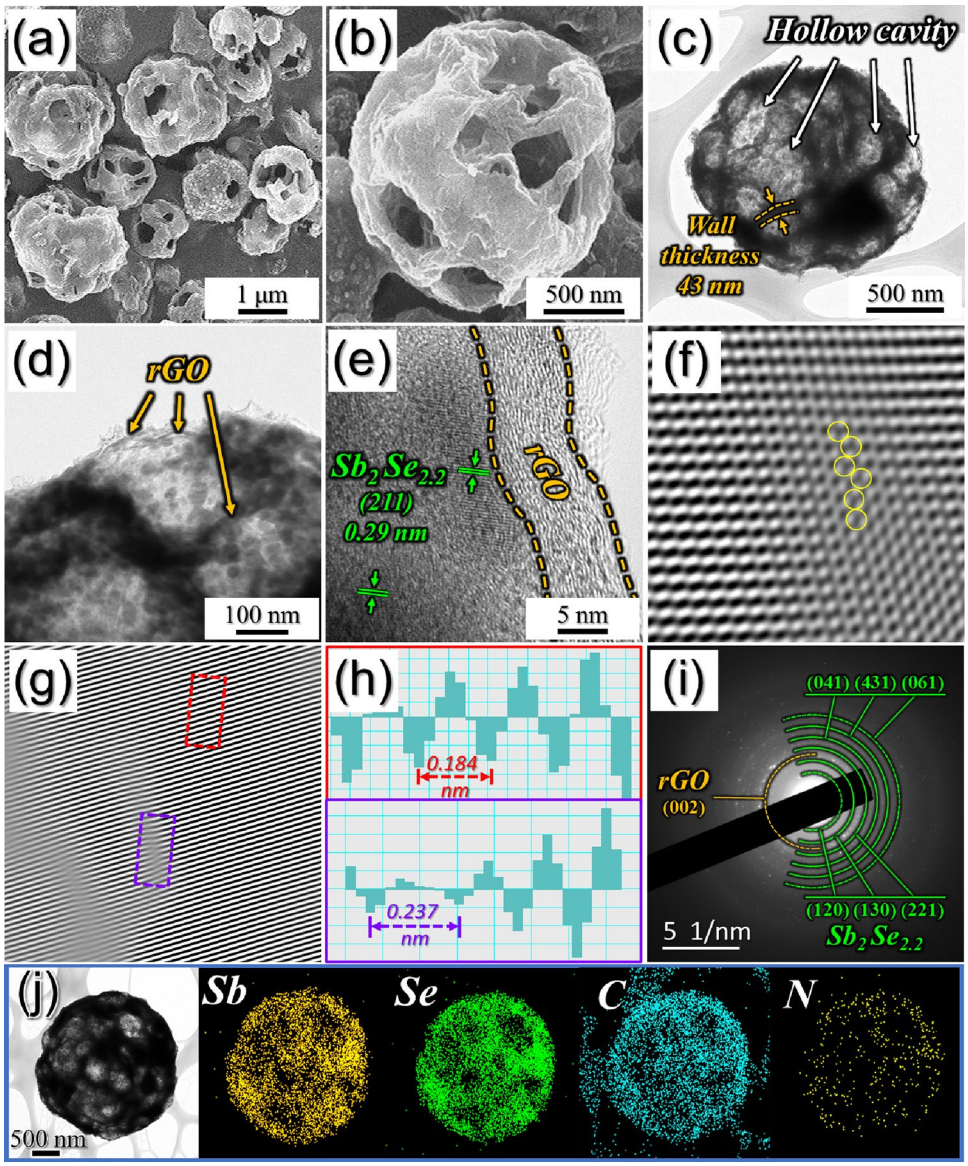

Fig. 4 Morphological and crystal structure characterizations of the H-$Sb_2Se_{2.2}$@rGO–600 microspheres obtained after selenization at 600 °C in reducing atmosphere: **a**, **b** FE-SEM micrographs, **c**, **d** TEM images, **e** HR-TEM image, **f**, **g** inverse FFT image (yellow circles in **f** mark defects), **h** lattice spacing profiles at selected areas (red and purple), **i** SAED pattern, and **j** elemental dot mapping images

drying of the droplets and their transformation into a more compact form (Scheme 1a-②). Furthermore, the organic units present in tartaric acid decompose completely into gaseous products, thus forming a hollow structure within the microspheres. The PS nanobeads underwent a complete thermal breakdown, leading to the formation of large, open cavities (Scheme 1a-③). Moreover, the Sb_2O_3 nanocrystals were partially reduced to metalloid Sb during spray pyrolysis. Likewise, the PVP polymer and GO nanosheets gradually reduced to the N-doped C matrix and rGO nanosheets, respectively. The rGO framework not only served as a conductive pathway for electron transmission but also enhanced the structural integrity of the microspheres. The as-sprayed powders then underwent a selenization process at 600 °C for 3 h, with a ramp rate of 5 °C min^{-1}, under a reducing atmosphere (5% H_2/Ar). The selenium powder was used to generate H_2Se gas. During the selenization process, the mixed Sb/Sb_2O_3 phase was initially converted to a stoichiometric Sb_2Se_3 phase (Scheme 1a-④). However, continued heating at high temperature during the selenization process resulted in the evaporation of Se from the crystal structure. This resulted in the formation of a Se-deficient selenide phase (Scheme 1a-⑤). As clearly shown in Scheme 1b, selenization at low temperature resulted in a typical selenide phase with an almost stoichiometric composition (Scheme 1b-①), whereas selenization at high temperature resulted in a high degree of atomic disorder owing to the formation of Se-defects or vacancies (Scheme 1b-②). This subsequently resulted in the formation of a non-stoichiometric composition. The functional interlayer obtained after coating the as-prepared nanostructures acted as a polysulfide

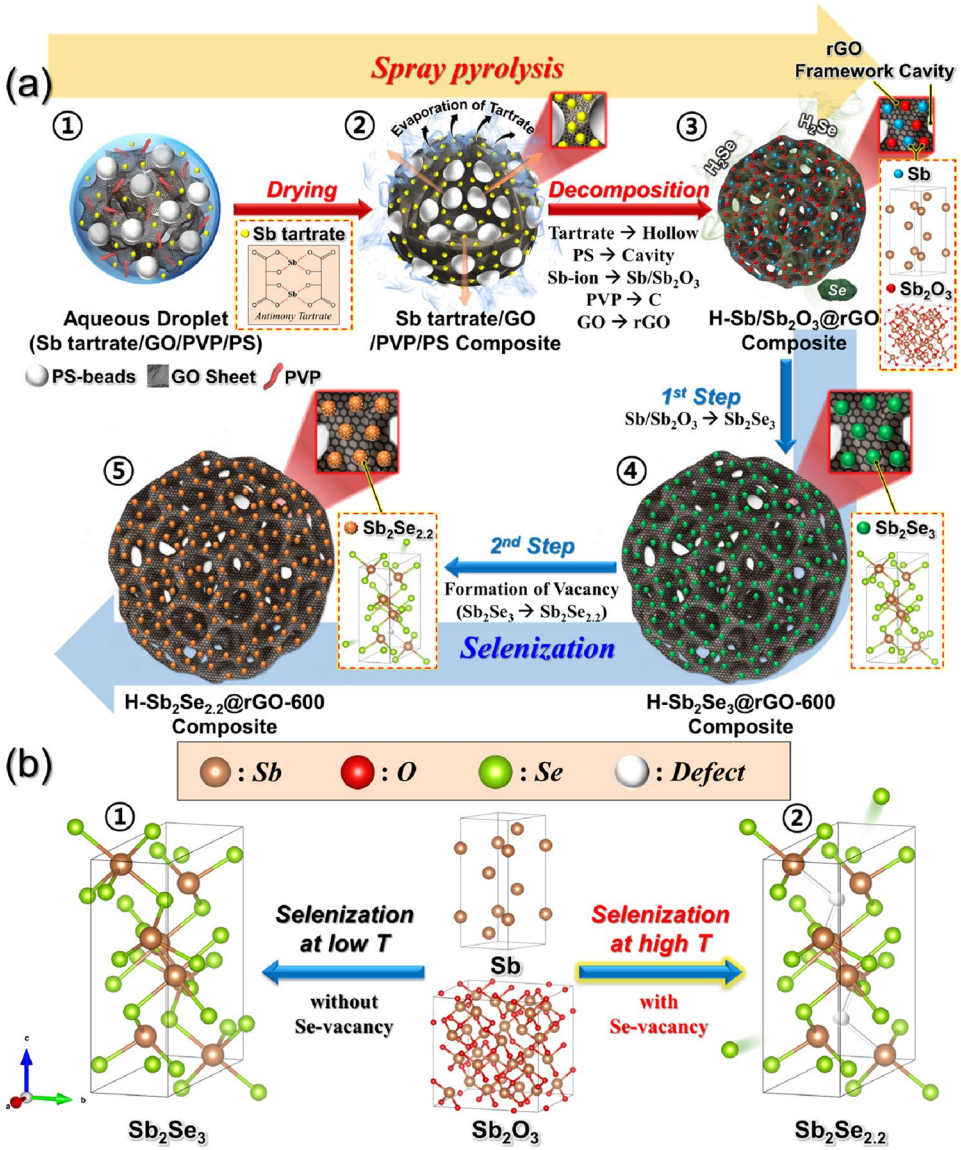

Scheme 1 **a** Schematic illustration of the formation mechanism of H-$Sb_2Se_{2.2}$@rGO–600 microspheres via facile spray pyrolysis technique (①–③) followed by selenization (④ and ⑤) at 600 °C for 3 h, and **b** illustration of temperature induced Se-defects to form non-stoichiometric $Sb_2Se_{2.2}$

storehouse to facilitate catalytic conversion of the trapped species, thus ensuring high active material utilization and an overall enhanced electrochemical performance.

X-ray photoelectron spectroscopy (XPS) was utilized to investigate the chemical state and bonding environment of the elements in the H-$Sb_2Se_{2.2}$@rGO−600 nanostructure. The XPS survey spectrum in Fig. 5a confirms the presence of Sb 3*d*, Se 3*d*, C 1*s*, and N 1*s* orbitals. The high-resolution Sb 3*d* and O 1*s* XPS spectra in Fig. 5b exhibit the Sb $3d_{5/2}$ and Sb $3d_{3/2}$ doublet states resulting from spin-orbit coupling [49, 50]. The additional O 1*s* peak at 532.4 eV indicates surface oxidation during the measurement [51]. Deconvolution of the Sb $3d_{5/2}$ and Sb $3d_{3/2}$ peaks reveals two main peaks at 528.5 and 537.8 eV, respectively, which are attributed to the Sb–Se bond in the Sb^{3+} environment [52]. The shoulder peaks at 529.7 and 538.7 eV are associated with surface oxidation and are assigned to Sb–O species [53, 54]. The high-resolution Se 3*d* XPS spectrum in Fig. 5c reveals two distinct peaks at 53.1 and 53.8 eV, corresponding to Se $3d_{5/2}$ and Se $3d_{3/2}$ electronic states, which are associated with Se–Sb bonding species [6]. Likewise, the fitted peaks at 55.2 and 55.9 eV are attributed to Se infiltration within the structure during selenization [55]. Additionally, the fitted, depressed peak centered at 57.9 eV corresponds to the Se–O species resulting from surface oxidation [56, 57]. Notably, the higher binding energy for the Se $3d_{5/2}$ and Se $3d_{3/2}$ electronic orbitals in H-$Sb_2Se_{2.2}$@rGO−600 compared to that of the Se $3d_{5/2}$ (52.6 eV) and Se $3d_{3/2}$ (53.6 eV) electronic orbitals for the selenized powder at 400 °C (Fig. S5a) can be attributed to the stronger Sb–Se bonds due to the absence of Se. The Sb 3*d* XPS spectrum in Fig. S5b also displays synchronized results. The deconvoluted C 1*s*

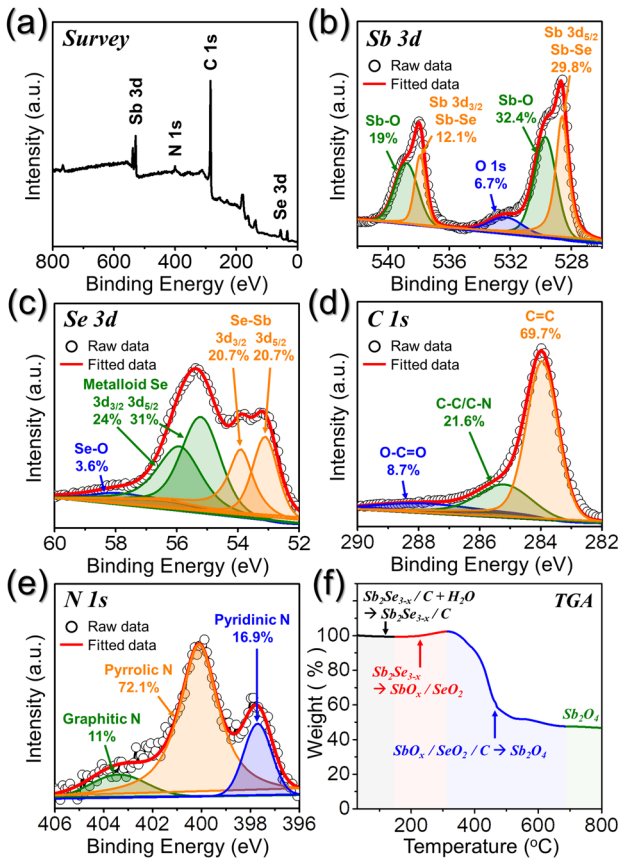

Fig. 5 **a** Survey spectrum, **b** Sb 3*d* XPS spectrum, **c** Se 3*d* XPS spectrum, **d** C 1*s* XPS spectrum, **e** N 1*s* XPS spectrum, and **f** TGA curve of H-$Sb_2Se_{2.2}$@rGO–600 microspheres in an air atmosphere

XPS spectrum (Fig. 5d) reveals three fitted photoelectron peaks at 283.9, 285.2, and 287.7 eV, corresponding to the –C=C–, –C–C/C–N–, and –O–C=O– bonding species, respectively [58–63]. Notably, the –C=C– peak exhibits the highest intensity, indicating the presence of the carbonaceous species in the nanostructure [64, 65]. Similarly, the –C–C/C–N– peak suggests the existence of doped N in the carbonaceous products, which is consistent with the elemental dot mapping results in Fig. 4j [66, 67]. The deconvoluted N 1*s* XPS spectrum shown in Fig. 5e displays three well-separated peaks at 397.7, 400.1, and 403.4 eV, which are attributed to pyridinic N, pyrrolic N, and graphitic N, respectively [5, 57, 68]. These results strongly validate the N-doping of the carbon framework. Notably, N-doping also contributes to enhancing the overall electronic conductivity of the nanostructure due to the higher electronegativity of N compared to that of C [56, 69]. The N 1*s* XPS results were further authenticated using elemental analysis (EA) results shown in Table S5, which indicate an N-content of ~1.0 wt% in H-$Sb_2Se_{2.2}$@rGO−600. To quantify the $Sb_2Se_{2.2}$ proportions in the prepared microspheres, a TG curve (Fig. 5f) was obtained. To reveal the phase of the sample after TG analysis, the H-$Sb_2Se_{2.2}$@rGO−600 sample was heated to 800 °C in an air atmosphere, and the leftover sample was analyzed (Fig. S6). The XRD pattern (Fig. S6b) shows that the carbon species completely decomposed in air, while the selenide phase converted to a residual oxide phase. Based on the EA, TG, and XRD results, the $Sb_2Se_{2.2}$ amount was ca. 74 wt%. Notably, the remaining 25 wt% of mass within the nanostructure consists of mainly C (19.7 wt%) and a negligible amount of moisture, organic elements in the form of hydrogen and sulfur impurities, and infiltrated Se into the carbon matrix. Furthermore, N_2 adsorption/desorption isotherms were obtained to analyze the specific surface area and pore-size distribution in the prepared nanostructure, as shown in Fig. S7. A BET surface area (Fig. S7a) of 21 m^2 g^{-1} was obtained for H-$Sb_2Se_{2.2}$@rGO−600. The BJH pore-size distribution curve in Fig. S7b features a maximum at ≈67 nm, which corresponds to the presence of large, open cavities within the nanostructure. Additionally, the sharp peak at 3.8 nm corresponds to the N_2 desorption tensile effect [17]. The porous structure facilitates electrolyte penetration and enables smooth diffusion of charge species, enhancing the redox processes.

The effect of the morphological and crystallographic characteristics of H-$Sb_2Se_{2.2}$@rGO−600 microspheres on enhancing the electrochemical performance of the Li–S cell was verified by testing stoichiometric antimony selenide (Sb_2Se_3) samples. The as-sprayed composite microspheres shown in Fig. S1 were sintered at a lower selenization temperature of 350 °C and subsequently examined using various physical characterization techniques, as shown in Fig. S8 (refer to the Supporting Information for a detailed discussion). Furthermore, another sample without the rGO and PS nanobead suspension was prepared as a standard reference. The physical characterization results of the as-sprayed and post-selenized sample (referred to as H-$Sb_2Se_{2.1}$−600 microspheres) are presented in Figs. S9 and S10, respectively.

2.4 Electrochemical performance of the prepared microspheres

The as-prepared hollow microspheres were employed as electrocatalytic interlayers by coating them onto a commercial separator to enhance the overall sulfur redox kinetics within the Li−S cells. The physical features of the separator coated with the H-$Sb_2Se_{2.2}$@rGO−600 microspheres are depicted in Fig. S11. The cross-sectional image in Fig. S11a demonstrates a uniform coating of the nanostructure on the separator, with a thickness of ≈3 µm. Additionally, a magnified FE-SEM image of the cross-section in Fig. S11b reveals a uniform coating of the H-$Sb_2Se_{2.2}$@rGO−600 microspheres and super-P on the surface of the separator. The FE-SEM micrograph of the pristine Celgard separator in Fig. S11c indicates numerous submicron openings, which

ensure efficient electrolyte penetration and smooth diffusion of charged species during the electrochemical process. To evaluate the overall improvement in the electrochemical performance, coin cells (CR2032-type) were assembled using conventional S electrodes, a Li anode, and coated separators as multifunctional electrocatalytic interlayers. Notably, considering the separator loading, the effective sulfur content in the cathode region was ca. 60.4%. CV tests were conducted on Li−S cells featuring the H-$Sb_2Se_{2.2}$@rGO−600, H-Sb/Sb_2Se_3@rGO−350, and H-$Sb_2Se_{2.1}$−600 microspheres as coated separators, as depicted in Fig. 6a. During the initial cathodic scan at 0.2 mV s^{-1}, all cells exhibited a typical two-step sulfur reduction process. The reduction peak labeled R1 corresponds to the reduction of elemental sulfur to highly soluble LiPSs (Li_2S_x, $4 \le x \le 8$), while reduction peak R2 indicates further reduction to the insoluble solid Li_2S_2/Li_2S state [70]. The anodic scan features an oxidation peak labeled O, indicating the single-step oxidation of Li_2S_2/Li_2S back to elemental sulfur *via* Li_2S_x. Among the assembled cells, the Li−S cell containing the H-$Sb_2Se_{2.2}$@rGO−600-coated separator displayed sharp and high-intensity reduction peaks, suggesting improved redox kinetics and enhanced utilization of the active material. This observation was supported by the individual redox peak voltages and the corresponding voltage polarization (voltage difference between R1 and O), as shown in Fig. 6b. The Li−S cell paired with the H-$Sb_2Se_{2.2}$@rGO−600-coated separator exhibited the lowest polarization potential ($\Delta V = 330$ mV) compared with the H-Sb/Sb_2Se_3@rGO−350 ($\Delta V = 420$ mV) and H-$Sb_2Se_{2.1}$−600 ($\Delta V = 580$ mV) coated separators. The five initial CV profiles in Fig. S12 feature well-overlapped curves, indicating highly reversible and kinetically favored redox processes within the cells. To further demonstrate the superior redox kinetics of the Li−S cells featuring H-$Sb_2Se_{2.2}$@rGO−600-coated separator, CV curves at different voltage scan rates ranging from 0.1 to 0.5 mV s^{-1} were

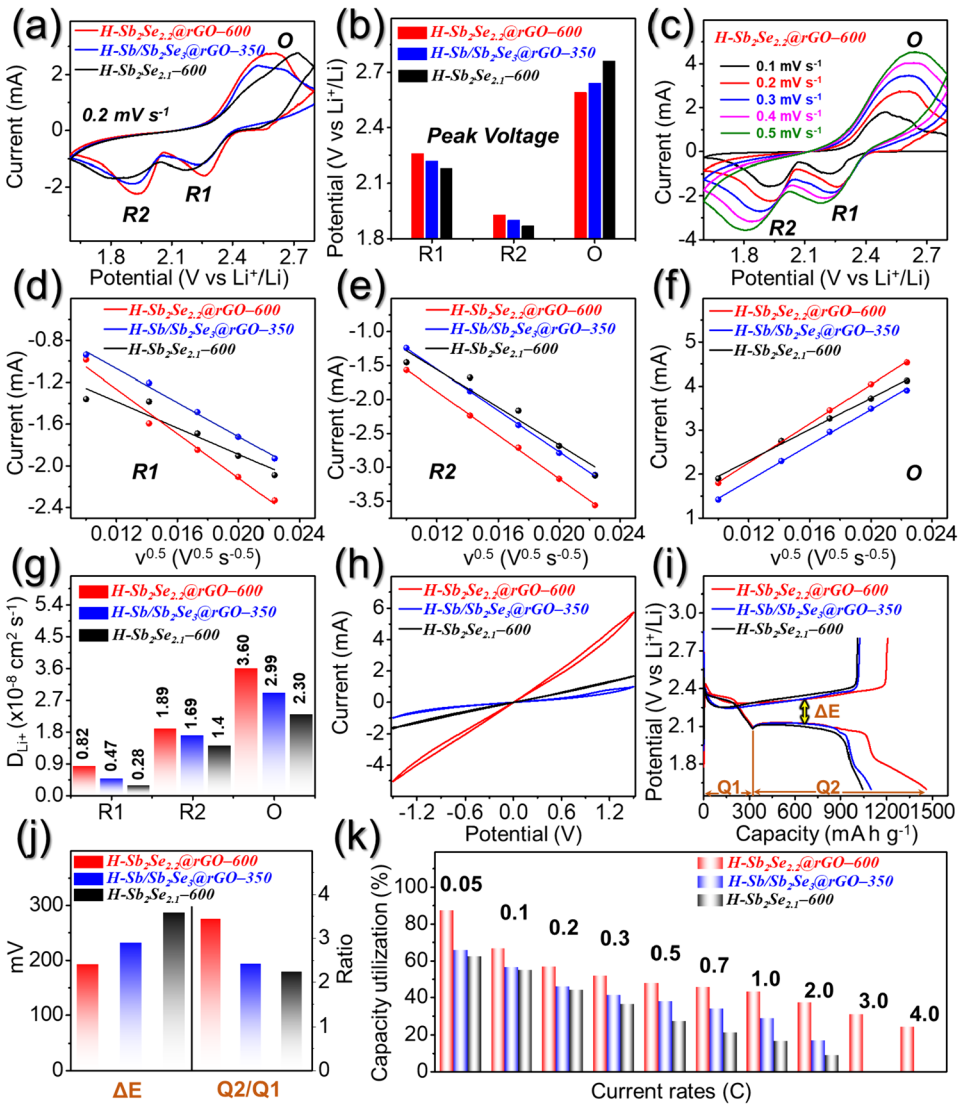

Fig. 6 **a** CV profiles of Li–S cells featuring different coated separator arrangements at 0.2 mV s^{-1}, **b** redox peak voltage comparison obtained from CV graphs, **c** CV profile at various voltage scan rates, **d–f** peak current vs. square root of the voltage scan rate plots for reduction and oxidation peaks, **g** lithium-ion diffusion coefficient (D_{Li}^{+}) values comparison, **h** comparison of electrocatalytic activity of as-prepared nanostructures using CV profiles from symmetric cells at a scan rate of 1.0 mV s^{-1}, **i** GCD voltage profiles of different coated separator arrangements at 0.05 C, **j** ΔE and Q2/Q1 comparison for different coated separators, and **k** capacity utilization at various C-rates

obtained and analyzed (Fig. 6c). The shape of the CV curves clearly indicates that the redox processes involved only S and Li_2S and have typical redox signatures, even at a high voltage scan rate of 0.5 mV s^{-1}. However, at high scan rates, the current intensity increased, and greater voltage hysteresis occurred. The CV curves for the Li−S cells incorporating the H-Sb/Sb_2Se_3@rGO−350 and H-$Sb_2Se_{2.1}$−600-coated separators (Fig. S13) exhibit similar redox characteristics, but the current intensity and voltage hysteresis varied, suggesting different extents of the redox reactions. The diffusion kinetics within the assembled cells were evaluated using the well-known Randles–Sevcik equation [7]:

$$I_p = 2.69 \times 10^5 n^{1.5} A\, D_{\mathrm{Li}^+}^{0.5}\, C_{\mathrm{Li}}\, v^{0.5} \quad (1)$$

where I_p is the redox current intensity, n is the quantity of electrons participating in redox reactions, A is the surface area of electrode (in cm^2), C_{Li} is the concentration of Li-ions (in mol L^{-1}), whereas v represents the scan rate (in V s^{-1}). The Li-ion diffusion coefficient ($D_{Li}{}^+$) was calculated for all Li−S cells using the slope obtained from the I_p vs. $v^{0.5}$ curves for three redox peaks (i.e., R1, R2, and O), as shown in Fig. 6d–f. The obtained $D_{Li}{}^+$ values are summarized in Fig. 6g. The Li−S cell featuring the H-$Sb_2Se_{2.2}$@rGO−600 displayed higher $D_{Li}{}^+$ values than the cells containing the H-Sb/Sb_2Se_3@rGO−350 and H-$Sb_2Se_{2.1}$−600-coated separators, indicating its improved reaction kinetics. This improvement is primarily attributed to the robust nanostructure engineering strategy, which ensured structural integrity and promoted synergetic effects. For instance, the high degree of atomic disorder in non-stoichiometric $Sb_2Se_{2.2}$ induced by Se-vacancies or defects enhances the polar electrophilic coupling interactions of $Sb^{\delta+} - S_x^{2-}$ and $Li^+ - Se^{\delta-}$, as validated by the DFT results in Fig. 2. Additionally, the N-doped carbonaceous species in the form of the self-supporting rGO framework guarantee fast electron transport during the electrochemical process. The enhanced coupling interactions were further verified *via* theoretically (DFT calculations) as well as experimentally (i.e., by conducting the static polysulfide adsorption tests). The DFT calculations in Fig. S14 clearly revealed that the charge accumulation for 2 Se-atom defective Sb_2Se_{3-x} (120) surface (Fig. S14b) is more active compared to the pristine Sb_2Se_3 (120) surface (Fig. S14a), when Li_2S_6 was adsorbed. Likewise, the Li−Se and Sb−S bond length values in Table S6 are far less for the defective Sb_2Se_{3-x} (120) surface, indicating enhanced coupling interaction between the polysulfide species and the defective surface. These theoretical results match well with the static polysulfide adsorption tests for various as-prepared microspheres, as shown in Fig. S15. The Li_2S_6 polysulfide solution was prepared according to our previous report [5]. As observed, the polysulfide solution containing microspheres with Se-induced defects (marked as "2" and "4") displays a more transparent solution compared to the solution containing stoichiometric powder (marked as "3"). These results again authenticate that the atomic disorder in the form of Se-defects provides additional sites for efficient anchoring of polysulfide species. These results are further supported by examining symmetric cell configurations to explore the electrocatalytic conversion effect of all the prepared nanostructures. The initial CV curve within the voltage window of −1.5 to 1.5 V (Fig. 6h) clearly indicates that the symmetric cell featuring the H-$Sb_2Se_{2.2}$@rGO−600 microspheres as both the counter and working electrode exhibits the highest current intensity, which explains its effective electrocatalysis towards LiPSs. By contrast, the symmetric cells containing H-Sb/Sb_2Se_3@rGO−350 and H-$Sb_2Se_{2.1}$−600 display weak electrocatalysis towards LiPSs. This is primarily due to the presence of well-entangled $Sb_2Se_{2.2}$ nanocrystals, which act as active chemisorption sites for efficient anchoring and electrocatalytic conversion of the trapped polysulfide species, thus ensuring high utilization of the active material. Overall, these results indicate the better electrochemical performance of the cells containing the H-$Sb_2Se_{2.2}$@rGO–600 microspheres compared to those containing H-Sb/Sb_2Se_3@rGO−350 and H-$Sb_2Se_{2.1}$−600. This is attributed to its nanostructural advantages, such as the defect-engineered nanostructure, porous framework, highly conductive skeleton, and the presence of polar chemisorption sites.

Further electrochemical characterizations were conducted to confirm the enhancement in redox processes resulting from the atomic irregularities in the crystal structure. Figure 6i reveals the initial galvanostatic charge–discharge (GCD) voltage profile at 0.05 C for different coated separator arrangements. The profiles exhibited two discharge voltage plateaus and a sloppy charging profile, indicating multistep sulfur redox processes that aligned with the CV curves in Fig. 6a. However, the lengths of the redox voltage plateaus varied among the different arrangements, suggesting uneven redox kinetics inside the cells. Among all the assembled Li−S cells, the cell incorporating the H-$Sb_2Se_{2.2}$@rGO−600-coated separator exhibited the longest redox voltage plateau length and lowest voltage polarization (denoted as ΔE), measured between the second reduction and oxidation voltage plateau. The calculated ΔE values are summarized in Fig. 6j, revealing that the H-$Sb_2Se_{2.2}$@rGO−600-coated separator exhibited a lower polarization ($\Delta E = 192$ mV) than the H-Sb/Sb_2Se_3@rGO−350 ($\Delta E = 232$ mV) and H-$Sb_2Se_{2.1}$−600 ($\Delta E = 286$ mV) coated separators. Furthermore, two independent variables, Q1 and Q2, and their relative ratio (Q2/Q1) were measured. Q1, the discharge capacity (theoretical value = 419 mA h g^{-1}) associated with the first discharge plateau and sloppy region, is related to the amount of LiPS formed and its diffusion towards the anode. Similarly, Q2, the discharge capacity (theoretical

value = 1256 mA h g^{-1}) associated with the second discharge plateau and subsequent sloppy region, indicates the efficient conversion of LiPS to Li_2S. Therefore, the Q2/Q1 ratio (theoretical value = 3) represents the electrocatalytic conversion capability of the prepared nanostructure. A higher Q2/Q1 guarantees better catalytic conversion of the trapped polysulfide species. The cell containing the H-$Sb_2Se_{2.2}$@rGO−600-coated separator exhibited the highest Q2/Q1 ratio (3.44) compared with those containing the H-Sb/Sb_2Se_3@rGO−350 (Q2/Q1 = 2.42) and H-$Sb_2Se_{2.1}$−600 (Q2/Q1 = 2.24) separators. This suggests that the cell containing the H-$Sb_2Se_{2.2}$@rGO−600 microspheres has a better electrocatalytic activity towards the lithium polysulfide species than the other two cells. However, the values were slightly higher than the theoretical analogs due to excess capacity (Q2) from the $LiNO_3$ reduction below 1.7 V during the initial cycle. Correspondingly, the cells incorporating the H-$Sb_2Se_{2.2}$@rGO−600-, H-Sb/Sb_2Se_3@rGO−350-, and H-$Sb_2Se_{2.1}$−600-coated separators showed an initial discharge capacity of 1460 mA h g^{-1} (87.2% of the theoretical value), 1097 mA h g^{-1} (65.5% of the theoretical value), and 1041 mA h g^{-1} (62.1% of the theoretical value), respectively. The superior discharge capacity of the cell incorporating the H-$Sb_2Se_{2.2}$@rGO−600-coated separator was clear evidence of kinetically favored reactions derived from the thermally induced Se-vacancies, which eventually resulted in enhanced polar electrophilic coupling interactions between non-stoichiometric $Sb_2Se_{2.2}$ and polysulfide species and thus high active material utilization. Besides, the highly conductive and porous framework supported fast redox kinetics *via* rapid charge transfer and smooth diffusion of charged species.

The rate performance of Li−S cells containing H-$Sb_2Se_{2.2}$@rGO−600, H-Sb/Sb_2Se_3@rGO−350, and H-$Sb_2Se_{2.1}$−600 coating arrangements at various C-rates ranging from 0.05 to 4.0 C is presented in Figs. 3f and S16. The cell containing the H-$Sb_2Se_{2.2}$@rGO−600-coated separator (Fig. 3e) exhibits well-distinguished charge−discharge voltage plateaus, even at a high C-rate of 4.0 C, which resulted in high discharge capacities at all C-rates, as shown in Fig. 3f. For instance, initial discharge capacities of 1460, 1112, 952, 865, 799, 761, 722, 622, 515, and 408 mA h g^{-1} were obtained at 0.05, 0.1, 0.2, 0.3, 0.5, 0.7, 1.0, 2.0, 3.0, and 4.0 C, respectively, for the H-$Sb_2Se_{2.2}$@rGO−600-coated separator cell, while initial discharge capacities of 1097/1041, 943/917, 765/736, 692/610, 631/451, 564/355, 475/276, 282/149, 20/42, and 12/19 mA h g^{-1}, respectively, were obtained at identical C-rates for the H-Sb/Sb_2Se_3@rGO−350- and H-$Sb_2Se_{2.1}$−600-coated separator cells, respectively. When the current was reversed to 0.1 C, the recovered specific discharge capacity for the H-$Sb_2Se_{2.2}$@rGO−600-coated separator (960 mA h g^{-1}) was higher than those of the H-Sb/Sb_2Se_3@rGO−350 (770 mA h g^{-1}) and H-$Sb_2Se_{2.1}$−600 (799 mA h g^{-1}) coated separator interlayers, indicating high reversibility of the redox processes. Furthermore, the capacity utilization values were calculated at different C-rates for various coated separator arrangements and are summarized in Fig. 6k. Generally, capacity utilization is a direct measurement of the amount of active material consumed during the redox reaction. As predicted, the H-$Sb_2Se_{2.2}$@rGO−600-coated separator cell exhibited the highest capacity utilization values among all the cells. The high active material utilization is consistent with the CV results, which predicted the lowest voltage hysteresis and superior electrocatalytic conversion capability.

The cycling performances of the assembled cells were assessed at low (0.1 C and 0.5 C) and high (1.0 and 4.0 C) C-rates. Figure 7a shows the cycling performances of the assembled cells with different coating separator arrangements at 0.1 C for 200 cycles. The cell containing the H-$Sb_2Se_{2.2}$@rGO−600-coated separator exhibited a higher initial discharge capacity (1225 mA h g^{-1}) than the cells containing the H-Sb/Sb_2Se_3@rGO−350 (977 mA h g^{-1}) and H-$Sb_2Se_{2.1}$−600 (1003 mA h g^{-1}) coated separators. However, after 200 cycles, 74.5% of the initial capacity was retained for the H-$Sb_2Se_{2.2}$@rGO−600-coated separator (912 mA h g^{-1}). By contrast, the H-Sb/Sb_2Se_3@rGO−350- and H-$Sb_2Se_{2.1}$−600-coated separators retained 41.8% (409 mA h g^{-1}) and 59.7% (599 mA h g^{-1}), respectively, of their initial capacities. In addition, the average capacity decay rate per cycle of the H-$Sb_2Se_{2.2}$@rGO−600-coated separator (0.10%) was lower than those of the H-Sb/Sb_2Se_3@rGO−350 (0.29%) and H-$Sb_2Se_{2.1}$−600 (0.20%) coated separators. The low-capacity decay rate for the H-$Sb_2Se_{2.2}$@rGO−600-coated separator was due to the availability of higher surface chemisorption sites generated due to a higher degree of atomic disorder in the form of Se-vacancies compared with H-Sb/Sb_2Se_3@rGO−350 and H-$Sb_2Se_{2.1}$−600. Moreover, the high Coulombic efficiencies throughout cycling suggest highly reversible redox processes inside the cell. The high-capacity retention values for the H-$Sb_2Se_{2.2}$@rGO−600 microspheres confirm the efficient LiPS anchoring within the cathodic domain, thus minimizing active material loss during prolonged cycling. Similar trends were observed for the Li−S cell featuring the H-$Sb_2Se_{2.2}$@rGO−600-coated separator cycled at 0.5 and 1.0 C, as shown in Fig. 7b and c, respectively. For instance, the cell featuring the H-$Sb_2Se_{2.2}$@rGO−600-coated separator exhibited an initial discharge capacity of 1030 mA h g^{-1} at 0.5 C (Fig. 7b) and maintained almost 64% (655 mA h g^{-1}) of its capacity after 220 cycles, with an average capacity decay rate of 0.16% per cycle. Similarly, at 1.0 C (Fig. 7c), the cell delivered an initial capacity of 707 mA h g^{-1}, which stabilized to 486 mA h g^{-1} (68.7% retention) after 200 continuous cycles (average decay rate of 0.15%). By contrast, the cell containing the H-Sb/Sb_2Se_3@rGO−350- and

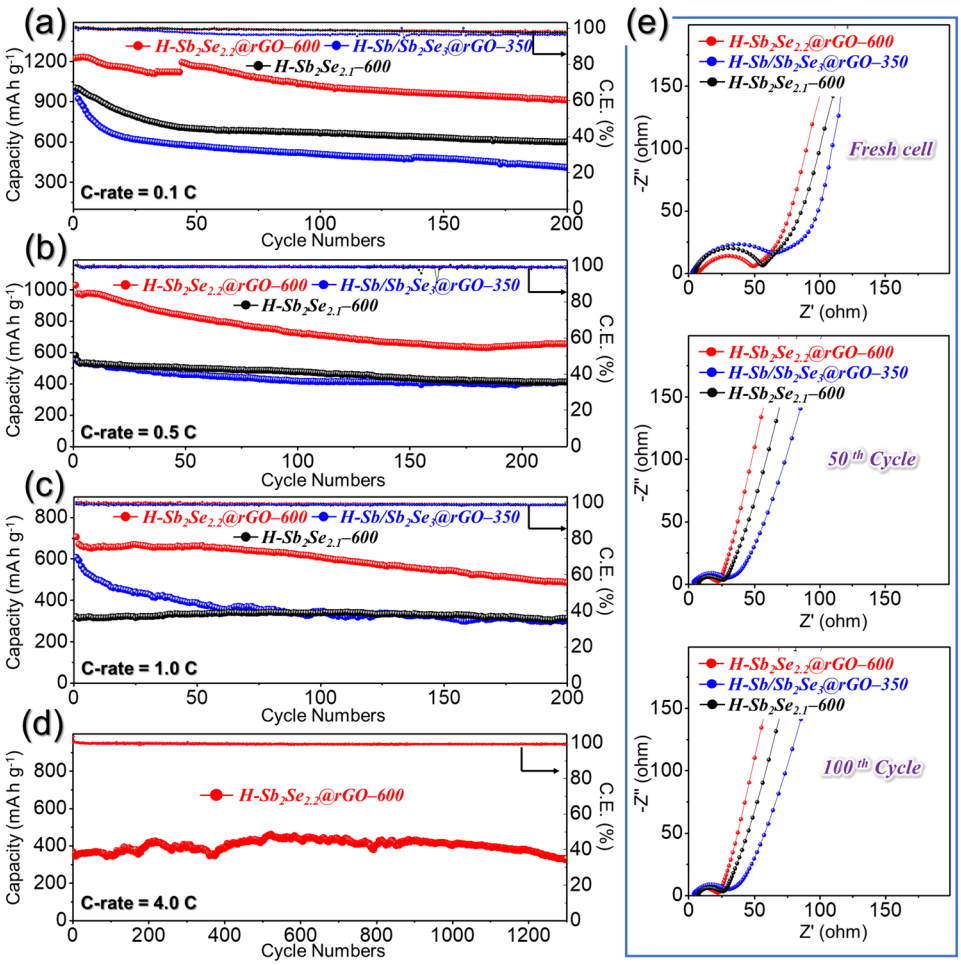

Fig. 7 Cycling performance of Li–S cells featuring different coated separators at **a** 0.1 C, **b** 0.5 C, **c** 1.0 C, **d** long-term cycling performance of H-$Sb_2Se_{2.2}$@rGO−600 at 4.0 C, and **e** Nyquist plots at different cycle numbers during cycling at 1.0 C

H-$Sb_2Se_{2.1}$−600-coated separators displayed inferior cycling performances at 0.5 and 1.0 C, suggesting continuous loss of the active material. The structural merits of the H-$Sb_2Se_{2.2}$@rGO−600 microspheres were further tested *via* prolonged cycling at a high C-rate of 4.0 C, as shown in Fig. 7d. The cell demonstrated an overwhelming cycling stability, with a capacity retention of 90.4% (an average capacity decay rate of just 0.007% per cycle), even after 1300 continuous charge−discharge cycles. The prolonged cycling stability result is consistent with the inference that the Se-vacancies induced nanostructural advantages in the H-$Sb_2Se_{2.2}$@rGO−600 microspheres, facilitated an effective polysulfide species capture, and suppressed active material loss. The improved redox kinetics owing to the highly conductive rGO framework facilitated smooth diffusion of charged species, whereas the porous skeleton ensured effective absorption of undesired volume fluctuations during the electrochemical processes.

We employed electrochemical impedance spectroscopy (EIS) to better understand the enhancement in the electrochemical performance and redox kinetics within the prepared nanostructures. Figure 7e shows the Nyquist plots obtained at different cycle numbers during cycling at a C-rate of 1.0 C in the charge state. The EIS spectra of the fresh cells exhibited a depressed semicircle in the high-frequency region. The first intercept of the semicircle on the *x*-axis corresponds to the solution or electrolyte resistance (R_e). By contrast, the second intercept represents the charge transfer resistance (R_{ct}), and the inclined line in the low-frequency region is associated with Li^+-ion diffusion. The cell with the H-$Sb_2Se_{2.2}$@rGO−600-coated separator exhibited a lower R_{ct} (≈43 Ω) than the cells containing the H-Sb/Sb_2Se_3@rGO−350 (≈75 Ω) and H-$Sb_2Se_{2.1}$−600 (≈54 Ω) coated separators. Even during cycling (after the 50th and 200th cycle), the R_{ct} values remained the lowest for the H-$Sb_2Se_{2.2}$@rGO−600-coated separator cell, mainly due to better electrolyte penetration and its highly conductive framework, which resulted in smooth diffusion of charged species. For instance, at the end of the 100th cycle, the H-$Sb_2Se_{2.2}$@rGO−600-coated separator still exhibited a lower R_{ct} (≈17 Ω) than the H-Sb/Sb_2Se_3@rGO−350 (≈30 Ω) and H-$Sb_2Se_{2.1}$−600 (≈21 Ω) coated separators. The lower R_{ct} values strongly indicate favorable redox kinetics that promoted faster electrocatalytic

conversion of polysulfides during the electrochemical processes.

As a multifunctional cathodic interlayer, the H-$Sb_2Se_{2.2}$@rGO−600-coated separator was further evaluated with more practical cell parameters, i.e., extremely high effective S content (65 and 66%), high active material loading (4.5 and 6.0 mg cm^{-2}), and lean E/S ratio (5.7 and 4.3 µL mg^{-1}). The obtained electrochemical results are presented in Fig. 8. The Li−S cell with a high-loaded S-electrode (4.5 mg cm^{-2}) displayed considerable rate capability performance (Fig. 8a). The cell exhibited a discharge capacity of 1076, 901, 738, 662, 598, and 583 mA h g^{-1} at C-rates of 0.05, 0.1, 0.15. 0.2, 0.25, and 0.3 C, respectively. When the current was reversed, the cell recovered the initial capacity values at 0.1 C. The GCD voltage profiles in Fig. 8b indicate that the typical voltage plateaus involving two-step sulfur redox reactions remained intact. The cells were further subjected to the cycling performance at 0.1 C, as shown in Fig. 8c. For an active material loading and E/S of 4.5 mg cm^{-2} and 5.7 µL mg^{-1}, respectively, the cell exhibited a first discharge capacity of 908 mA h g^{-1} at 0.1 C. After 120 continuous cycles, a discharge capacity of 815 mA h g^{-1} (89% retention) was still obtained, with an average capacity decay rate of just 0.08%. Similar trends were observed when the sulfur loading and E/S were changed to 4.3 mg cm^{-2} and 6.0 µL mg^{-1}, respectively. The cell exhibited a discharge capacity of 872 mA h g^{-1} after 120 continuous cycles, indicating an average capacity decay rate of 0.05%. The above electrochemical results suggest that even with more feasible parameters, the Li−S cells exhibited extremely stable sulfur redox processes, primarily owing to the robust nanostructures and favorable electrophilic adsorption sites in the form of Se-vacancies in the H-$Sb_2Se_{2.2}$@rGO−600 microspheres. Figure 8d and Table S7 summarize previously reported electrochemical performances based on various practical parameters and compare them with the present work. As observed in Fig. 8d, the cell performance was superior or comparable to those obtained in previous studies, particularly considering the high effective S content and low E/S ratio. To validate these findings, the cycled cells (Fig. 8c) were used to power a light-emitting diode (10 mW, 5 V) patterned with "CBNU," as illustrated in Fig. 8e. The series

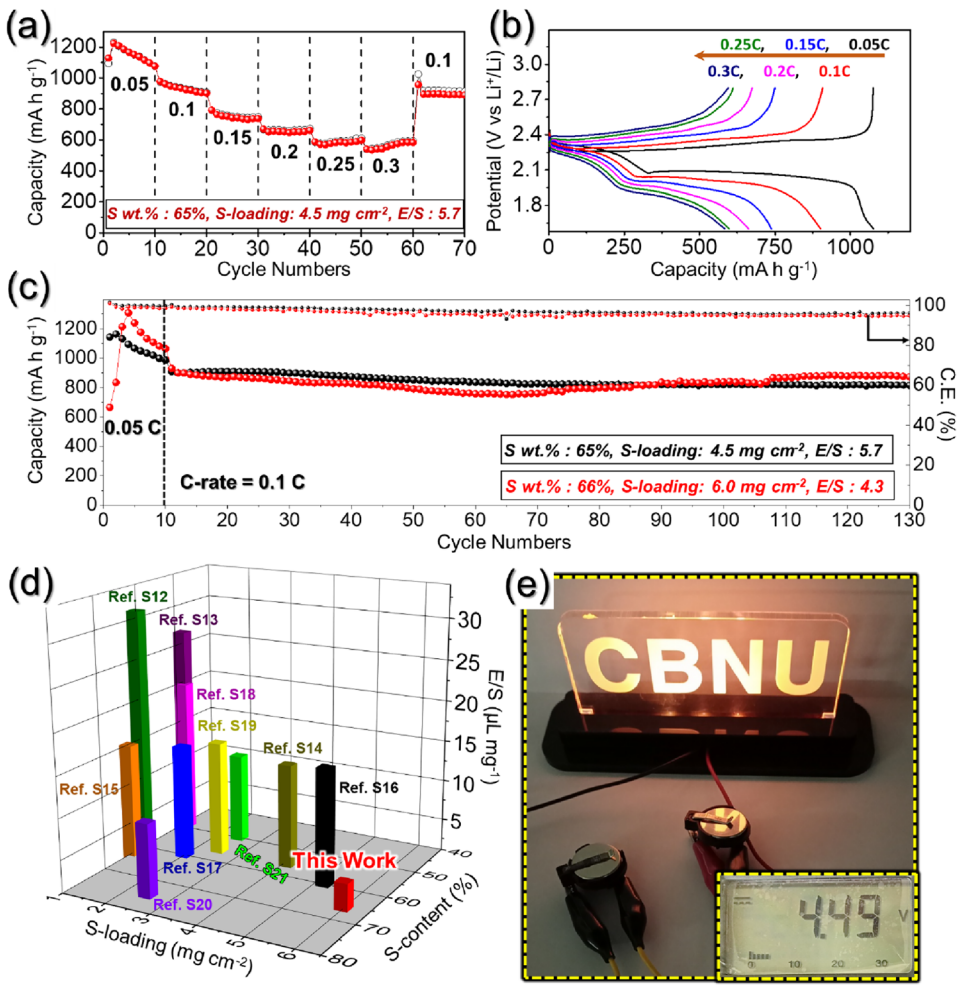

Fig. 8 **a** Rate capability results of Li−S featuring high-loading electrodes and H-$Sb_2Se_{2.2}$@rGO−600-coated separator, **b** respective GCD voltage profiles at various C-rates ranging from 0.05 to 0.3 C, **c** cycling performance with different cell parameters at 0.1 C, **d** comparison of the electrochemical performance obtained in this work to the previous reports, and **e** digital image of a light-emitting diode (5 V, 10 mW) powered by two cells utilized after cycling performance tests at 0.1 C

cell combination delivered uninterrupted power to the load for 0.5 h, confirming its suitability for practical applications. This again proved that the disordered structural advantages in the H-$Sb_2Se_{2.2}$@rGO−600 microspheres enhanced the efficient immobilization of active material in the cathodic region and promoted an efficient electrocatalytic conversion. To verify the stability of highly disordered atomic and unsaturated catalytic sites caused by Se-vacancies during cycling, the Li–S cell was disassembled after 200 cycles at 1.0 C and the H-$Sb_2Se_{2.2}$@rGO–600 material was characterized using HR-TEM, as shown in Fig. S17. The HR-TEM image (Fig. S17a) and FFT pattern (inset) demonstrate that the orthorhombic crystal structure remains intact. Besides, the IFFT image (Fig. S17b and c) and lattice spacing profile (Fig. S17d) confirm that atomic defects and edge dislocations are sustained even after the cycling, revealing that improved redox kinetics inside the Li–S cells are mainly defects administered. Therefore, our results demonstrate that the rational defect engineering strategy presented in this study could be adopted for more practical applications of LSBs, even under severe battery parameters.

3 Conclusions

In summary, we synthesized non-stoichiometric antimony selenide nanocrystals well-embedded in an rGO matrix constituting 3D hollow microspheres (H-$Sb_2Se_{2.2}$@rGO–600). We accurately controlled the heating conditions and used this material as a coating interlayer at the cathode side of Li–S cells, which enhanced the overall electrochemical performance. DFT calculations clearly indicated that the thermally induced crystal disorder in the form of Se-defects enhances the polar electrophilic coupling interactions of $Sb^{\delta+} - S_x^{2-}$ and $Li^{+} - Se^{\delta-}$, thus lowering the shuttling process and allowing kinetically favored redox processes. In addition, the self-supporting rGO framework provides numerous conductive pathways for fast electron transfer during the electrochemical process besides stabilizing the 3D hollow nanostructure. The decomposition of tartaric acid resulted in the formation of a hollow structure, whereas cavities were introduced using a PS-nanobead-based suspension. The hollow structure with open cavities offers smooth diffusion of charged species by shortening the effective charge-diffusion length, lowering the overall electrolyte volume consumption inside the cell, and channelizing the severe volume variations during the lithiation/delithiation processes. Correspondingly, the Li–S batteries incorporating the regular sulfur electrode and H-$Sb_2Se_{2.2}$@rGO−600-coated separator demonstrated excellent rate capabilities (up to 4.0 C) and remarkable cycling stability, that is, a capacity retention of 90.4% with an average capacity decay rate of just 0.007% per cycle, even after 1300 continuous charge−discharge cycles at 4.0 C. Even under more demanding cell conditions, such as high effective sulfur content (66%), high sulfur loading (6.0 mg cm^{-2}), and a low E/S ratio (4.3 µL mg^{-1}), the cell exhibited an impressive cycling stability of 120 cycles at 0.1 C, along with a feasible rate performance up to 0.3 C. Overall, the structural and electrochemical advancements demonstrated in this study will provide valuable insights for the synthesis of defect-engineered, stable nanostructures for efficient catalysis and adsorption in highly durable LSBs.

Supplementary information The online version contains supplementary material available at https://doi.org/10.1007/s42114-024-00892-9.

Author contributions Rakesh Saroha—designed the idea, performed experiments, and prepared the initial blueprint. Dong Yun Shin—DFT calculations and analysis. Jae Seob Lee and Sung Woo Cho—performed experiments and data accumulation. Dong-Hee Lim—DFT analysis, review and editing. Jung Sang Cho—supervision, writing, review and editing.

Funding This work was supported by the National Research Foundation of Korea (NRF) and funded by the Korean Government (MSIP) (grant numbers No. RS-2023-00217581 and NRF-2021R1I1A3057700). This work was partly supported by the Korea Institute of Energy Technology Evaluation and Planning (KETEP) grant funded by the Korea government (MOTIE) (20224000000070, Human Resource Training for Smart Energy New Industry Cluster). This research was supported by the "Regional Innovation Strategy (RIS)" through the National Research Foundation of Korea (NRF) funded by the Ministry of Education (MOE) (2021RIS-001).

Data availability The data are available from the corresponding author upon reasonable request.

Declarations

Competing interests The authors declare no competing interests.

References

1. Li Q, Li G, Fu C, Luo D, Fan J, Li L (2014) K^+-doped $Li_{1.2}Mn_{0.54}Co_{0.13}Ni_{0.13}O_2$: a novel cathode material with an enhanced cycling stability for lithium-ion batteries. ACS Appl Mater Interfaces 6(13):10330–10341. https://doi.org/10.1021/am5017649
2. Saroha R, Ahn J-H, Cho JS (2021) A short review on dissolved lithium polysulfide catholytes for advanced lithium-sulfur batteries. Korean J Chem Eng 38(1):461–474. https://doi.org/10.1007/s11814-020-0729-5
3. Jayasubramaniyan S, Lee H-W (2023) Directing battery chemistry using side-view operando optical microscopy. Korean J Chem Eng 40(1):488–496. https://doi.org/10.1007/s11814-022-1321-y
4. Kim JH, Kim BR, Im JS (2023) Optimization of the molecular weight range of coating pitch and its effect on graphite anodes for lithium-ion batteries. Korean J Chem Eng 40(1):2839–2846. https://doi.org/10.1007/s11814-023-1529-5
5. Saroha R, Oh JH, Seon YH, Kang YC, Lee JS, Cho JS (2021) Freestanding interlayers for Li-S batteries: design and synthesis of hierarchically porous N-doped C nanofibers comprising vanadium nitride quantum dots and MOF-derived hollow N-doped C

nanocages. J Mater Chem A 9(19):11651–11664. https://doi.org/10.1039/D1TA01802G
6. Son D, Lim W-G, Le J (2023) A short review of the recent developments in functional separators for lithium-sulfur batteries. Korean J Chem Eng 40(1):473–487. https://doi.org/10.1007/s11814-022-1372-0
7. Saroha R, Oh JH, Lee JS, Kang YC, Jeong SM, Kang D-W, Cho C, Cho JS (2021) Hierarchically porous nanofibers comprising multiple core–shell Co_3O_4@graphitic carbon nanoparticles grafted within N-doped CNTs as functional interlayers for excellent Li–S batteries. Chem Eng J 426(1):130805. https://doi.org/10.1016/j.cej.2021.130805
8. Zhang Z, Luo D, Li G, Gao R, Li M, Li S, Zhao L, Dou H, Wen G, Sy S, Hu Y, Li J, Yu A, Chen Z (2020) Tantalum-based electrocatalyst for polysulfide catalysis and retention for high-performance lithium-sulfur batteries. Matter 3(1):920–934. https://doi.org/10.1016/j.matt.2020.06.002
9. Saroha R, Cho JS (2022) Nanofibers comprising interconnected chain-like hollow N-doped C nanocages as 3D free-standing cathodes for Li–S batteries with super-high sulfur content and lean electrolyte/sulfur ratio. Small Methods 6(5):2200049. https://doi.org/10.1002/smtd.202200049
10. Saroha R, Heo J, Liu Y, Angulakshmi N, Lee Y, Cho K-K, Ahn H-J, Ahn J-H (2022) V_2O_3-decorated carbon nanofibers as a robust interlayer for long-lived, high-performance, room-temperature sodium–sulfur batteries. Chem Eng J 431(2):134205. https://doi.org/10.1016/j.cej.2021.134205
11. Chiochan P, Kaewruang S, Phattharasupakun N, Wutthiprom J, Maihom T, Limtrakul J, Nagarkar SS, Horike S, Sawangphruk M (2017) Chemical adsorption and physical confinement of polysulfides with the janus-faced interlayer for high-performance lithium-sulfur batteries. Sci Rep 7(1):17703. https://doi.org/10.1038/s41598-017-18108-0
12. Seon YH, Saroha R, Cho JS (2022) Hierarchically porous N-doped C nanofibers comprising TiO_2 quantum dots and ZIF-8-derived hollow C nanocages as ultralight interlayer for stable Li–S batteries. Compos B Eng 237(1):109856. https://doi.org/10.1016/j.compositesb.2022.109856
13. Yuan H, Liu T, Liu Y, Nai J, Wang Y, Zhang W, Tao X (2019) A review of biomass materials for advanced lithium–sulfur batteries. Chem Sci 10(32):7484–7495. https://doi.org/10.1039/C9SC02743B
14. Saroha R, Seon YH, Jin B, Kang YC, Kang D-W, Jeong SM, Cho JS (2022) Self-supported hierarchically porous 3D carbon nanofiber network comprising Ni/Co/$NiCo_2O_4$ nanocrystals and hollow N-doped C nanocages as sulfur host for highly reversible Li–S batteries. Chem Eng J 446(2):137141. https://doi.org/10.1016/j.cej.2022.137141
15. Saroha R, Heo J, Li X, Angulakshmi N, Lee Y, Ahn H-J, Ahn J-H, Kim J-H (2022) Asymmetric separator integrated with ferroelectric-$BaTiO_3$ and mesoporous-CNT for the reutilization of soluble polysulfide in lithium-sulfur batteries. J Alloys Compd 893(1):162272. https://doi.org/10.1016/j.jallcom.2021.162272
16. Jana M, Xu R, Cheng X-B, Yeon JS, Park JM, Huang J-Q, Zhang Q, Park H-S (2020) Rational design of two-dimensional nanomaterials for lithium–sulfur batteries. Energy Environ Sci 13(4):1049–1075. https://doi.org/10.1039/C9EE02049G
17. Saroha R, Ka HS, Cho JS (2022) A novel three-dimensional ordered mesoporous microspheres comprising N-doped graphitic carbon-coated Fe_xP nanoparticles as multifunctional interlayers to suppress polysulfide crossover in Li–S batteries. Appl Surf Sci 612(1):155892. https://doi.org/10.1016/j.apsusc.2022.155892
18. Yang Y, Zhong Y, Shi Q, Wang Z, Sun K, Wang H (2018) Electrocatalysis in lithium sulfur batteries under lean electrolyte conditions. Angew Chem 130(47):15775–15778. https://doi.org/10.1002/anie.201808311
19. Choi JM, Saroha R, Kim JS, Jang MR, Cho JS (2023) Porous nanofibers comprising VN nanodots and densified N-doped CNTs as redox-active interlayers for Li–S batteries. J Power Sources 559(1):232632. https://doi.org/10.1016/j.jpowsour.2023.232632
20. Yang SH, Choi JM, Saroha R, Cho SW, Kang YC, Cho JS (2023) Hollow porous carbon nanospheres containing polar cobalt sulfide (Co_9S_8) nanocrystals as electrocatalytic interlayers for the reutilization of polysulfide in lithium–sulfur batteries. J Colloid Interface Sci 645(1):33–44. https://doi.org/10.1016/j.jcis.2023.04.083
21. Liang Q, Wang S, Yao Y, Dong P, Song H (2023) Transition metal compounds family for Li–S batteries: the DFT-guide for suppressing polysulfides shuttle. Adv Funct Mater 33(32):2300825. https://doi.org/10.1002/adfm.202300825
22. Zhang P, Yue L, Liang Q, Gao H, Yan Q, Wang L (2023) A review of transition metal compounds as functional separators for lithium-sulfur batteries. ChemistrySelect 8(1):e202203352. https://doi.org/10.1002/slct.202203352
23. Liang X, Kwok CY, Lodi-Marzano F, Pang Q, Cuisinier M, Huang H, Hart HJ, Houtarde D, Kaup K, Sommer H, Brezesinski T, Janek J, Nazar LF (2016) Tuning transition metal oxide–sulfur interactions for long life lithium sulfur batteries: the Goldilocks principle. Adv Energy Mater 6(6):1501636. https://doi.org/10.1002/aenm.201501636
24. Chen Z, Lv W, Kang F, Li J (2019) Theoretical investigation of the electrochemical performance of transition metal nitrides for lithium–sulfur batteries. J Phys Chem C 123(41):25025–25030. https://doi.org/10.1021/acs.jpcc.9b04670
25. Chen L, Li X, Xu Y (2018) Recent advances of polar transition-metal sulfides host materials for advanced lithium–sulfur batteries. Funct Mater Lett 11(6):1840010. https://doi.org/10.1142/S1793604718400106
26. Zhang C, Cui L, Abdolhosseinzadeh S, Heier J (2020) Two-dimensional MXenes for lithium-sulfur batteries. InfoMat 2(4):613–638. https://doi.org/10.1002/inf2.12080
27. Wang H, Deng N, Wang S, Wang X, Li Y, Zeng Q, Luo S, Cui X, Cheng B, Kang W (2022) Advanced preparation and application of transition metal selenides in lithium-sulfur batteries: a review. J Mater Chem A 10(44):23433–23466. https://doi.org/10.1039/D2TA05576G
28. Huang S, Huixiang E, Yang Y, Zhang Y, Ye M, Li CC (2021) Transition metal phosphides: new generation cathode host/separator modifier for Li–S batteries. J Mater Chem A 9(12):7458–7480. https://doi.org/10.1039/D0TA11919A
29. Manzeli S, Ovchinnikov D, Pasquier D, Yazyev OV, Kis A (2017) 2D transition metal dichalcogenides. Nat Rev Mater 2(8):17033. https://doi.org/10.1038/natrevmats.2017.33
30. Wang M, Fan L, Wu X, Qiu Y, Guan B, Wang Y, Zhang N, Sun K (2019) Metallic $NiSe_2$ nanoarrays towards ultralong life and fast Li_2S oxidation kinetics of Li–S batteries. J Mater Chem A 7(25):15302–15308. https://doi.org/10.1039/C9TA03361K
31. Yang T, Zhou J, Song TT, Shen L, Feng YP, Yang M (2020) High-throughput identification of exfoliable two-dimensional materials with active basal planes for hydrogen evolution. ACS Energy Lett 5(7):2313–2321. https://doi.org/10.1021/acsenergylett.0c00957
32. Sun Y, Zhang X, Mao B, Cao M (2016) Controllable selenium vacancy engineering in basal planes of mechanically exfoliated WSe_2 monolayer nanosheets for efficient electrocatalytic hydrogen evolution. Chem Commun 52(99):14266–14269. https://doi.org/10.1039/C6CC07832J
33. Gong X, Li R, Chen H, He C, Gao Za, Xie H (2023) (111)-Oriented crystalline plane MnO loaded by biomass carbon separator to facilitate sulfur redox kinetics in lithium–sulfur batteries. Arab J Chem 16(6):104752. https://doi.org/10.1016/j.arabjc.2023.104752
34. Wen J, Pei Y, Liu L, Su D, Yang M, Wang Q, Zhang W, Dai J, Feng Y, Wu T, Wang X (2021) Fully encapsulated Sb_2Se_3/Sb/C

nanofibers: towards high-rate, ultralong-lifespan lithium-ion batteries. J Alloys Compd 874(1):159961. https://doi.org/10.1016/j.jallcom.2021.159961
35. Dong Y, Feng Y, Deng J, He P, Ma J (2020) Electrospun Sb_2Se_3@C nanofibers with excellent lithium storage properties. Chin Chem Lett 31(3):909–914. https://doi.org/10.1016/j.cclet.2019.11.039
36. Li C, Song H, Mao C, Peng H, Li G (2019) A novel MoS_2 nanosheets-decorated Sb@Sb_2S_3@C tubular composites as anode material for high performance lithium ion battery. J Alloys Compd 786(1):169–176. https://doi.org/10.1016/j.jallcom.2019.01.315
37. Fan G, Wang Z, Ren H, Liu Y, Fan R (2021) Dielectric dispersion of copper/rutile cermets: dielectric resonance, relaxation, and plasma oscillation. Scr Mater 190(1):1–6. https://doi.org/10.1016/j.scriptamat.2020.08.027
38. Fan G, Wang Z, Sun K, Liu Y, Fan R (2021) Doped ceramics of indium oxides for negative permittivity materials in MHz-kHz frequency regions. J Mater Sci Technol 61(1):125–131. https://doi.org/10.1016/j.jmst.2020.06.013
39. Saroha R, Panwar AK (2017) Effect of in situ pyrolysis of acetylene (C_2H_2) gas as a carbon source on the electrochemical performance of $LiFePO_4$ for rechargeable lithium-ion batteries. J Phys D: Appl Phys 50(25):255501. https://doi.org/10.1088/1361-6463/aa708c
40. Deng Z, Chen D, Tang F, Ren J, Muscat AJ (2009) Synthesis and purple-blue emission of antimony trioxide single-crystalline nanobelts with elliptical cross section. Nano Res 2(2):151–160. https://doi.org/10.1007/s12274-009-9014-y
41. Pattini F, Rampino S, Mezzadri F, Calestani D, Spaggiari G, Sidoli M, Delmonte D, Sala A, Gilioli E, Mazzer M (2020) Role of the substrates in the ribbon orientation of Sb_2Se_3 films grown by low-temperature pulsed electron deposition. Sol Energy Mater Sol Cells 218(1):110724. https://doi.org/10.1016/j.solmat.2020.110724
42. Yin L-C, Liang J, Zhou G-M, Li F, Saito R, Cheng H-M (2016) Understanding the interactions between lithium polysulfides and N-doped graphene using density functional theory calculations. Nano Energy 25(1):203–210. https://doi.org/10.1016/j.nanoen.2016.04.053
43. Zhang B, Wu J, Gu J, Li S, Yan T, Gao X-P (2021) The fundamental understanding of lithium polysulfides in ether-based electrolyte for lithium–sulfur batteries. ACS Energy Lett 6(2):537–546. https://doi.org/10.1021/acsenergylett.0c02527
44. Wang L, Hu Z, Wan X, Hua W, Li H, Yang QH, Wang W (2022) Li_2S_4 anchoring governs the catalytic sulfur reduction on defective $SmMn_2O_5$ in lithium–sulfur battery. Adv Energy Mater 12(20):2200340. https://doi.org/10.1002/aenm.202200340
45. Lim D-H, Wilcox J (2011) DFT-based study on oxygen adsorption on defective graphene-supported pt nanoparticles. J Phys Chem C 115(46):22742–22747. https://doi.org/10.1021/jp205244m
46. Zhang L, Xia Z (2011) Mechanisms of oxygen reduction reaction on nitrogen-doped graphene for fuel cells. J Phys Chem C 115(22):11170–11176. https://doi.org/10.1021/jp201991j
47. Li X, Paier J, Sauer J, Mirabella F, Zaki E, Ivars-Barceló F, Shaikhutdinov S, Freund H-J (2018) Surface termination of Fe_3O_4 (111) films studied by CO adsorption revisited. J Phys Chem B 122(2):527–533. https://doi.org/10.1021/acs.jpcb.7b04228
48. Zhang J, Li W, Wang J, Pu X, Zhang G, Wang S, Wang N, Li X (2023) Engineering p-band center of oxygen boosting H^+ intercalation in δ-MnO_2 for aqueous zinc ion batteries. Angew Chem Int Ed 62(8):e202215654. https://doi.org/10.1002/anie.202215654
49. Martini I, Chevallay E, Fedosseev V, Hessler C, Neupert H, Nistor V, Taborelli M (2015) Surface characterization at CERN of photocathodes for photoinjector applications. IPAC2015, Richmond, VA, USA (May)
50. Park J-S, Kang YC (2019) Uniquely structured sb nanoparticle-embedded carbon/reduced graphene oxide composite shell with empty voids for high performance sodium-ion storage. Chem Eng J 373(1):227–237. https://doi.org/10.1016/j.cej.2019.05.036
51. Bodenes L, Darwiche A, Monconduit L, Martinez H (2015) The solid electrolyte interphase a key parameter of the high performance of Sb in sodium-ion batteries: comparative X-ray photoelectron spectroscopy study of Sb/Na-ion and Sb/Li-ion batteries. J Power Sources 273(1):14–24. https://doi.org/10.1016/j.jpowsour.2014.09.037
52. Whittles TJ, Veal TD, Savory CN, Welch AW, de Souza Lucas FW, Gibbon JT, Birkett M, Potter RJ, Scanlon DO, Zakutayev A, Dhanak VR (2017) Core levels, band alignments, and valence-band states in $CuSbS_2$ for solar cell applications. ACS Appl Mater Interfaces 9(48):41916–41926. https://doi.org/10.1021/acsami.7b14208
53. Petit E, Riga J, Caudano R (1991) Surface and interface XPS characterization of the oxide layer grown on antimony under UV laser irradiation. Surf Sci 251–252(1):529–534. https://doi.org/10.1016/0039-6028(91)91049-4
54. Tang X, Van Welzenis R, Van Setten F, Bosch A (1986) Oxidation of the InSb surface at room temperature. Semicond Sci Technol 1(6):355. https://doi.org/10.1088/0268-1242/1/6/004
55. Seon YH, Kang YC, Cho JS (2021) One-dimensional porous nanostructure composed of few-layered $MoSe_2$ nanosheets and highly densified-entangled-N-doped CNTs as anodes for na ion batteries. Chem Eng J 425(1):129051. https://doi.org/10.1016/j.cej.2021.129051
56. Lee JS, Saroha R, Cho JS (2022) Porous microspheres comprising $CoSe_2$ nanorods coated with N-doped graphitic C and polydopamine-derived C as anodes for long-lived Na-ion batteries. Nano-Micro Lett 14(1):113. https://doi.org/10.1007/s40820-022-00855-z
57. Lee JS, Park J-S, Baek KW, Saroha R, Yang SH, Kang YC, Cho JS (2023) Coral-like porous microspheres comprising polydopamine-derived N-doped C-coated $MoSe_2$ nanosheets composited with graphitic carbon as anodes for high-rate sodium-and potassium-ion batteries. Chem Eng J 456(1):141118. https://doi.org/10.1016/j.cej.2022.141118
58. Lee JS, Jo MS, Saroha R, Jung DS, Seon YH, Lee JS, Kang YC, Kang D-W, Cho JS (2020) Hierarchically well-developed porous graphene nanofibers comprising N-doped graphitic C-coated cobalt oxide hollow nanospheres as anodes for high-rate Li-ion batteries. Small 16(32):2002213. https://doi.org/10.1002/smll.202002213
59. Lee JS, Saroha R, Oh SH, Shin DH, Jeong SM, Kim JK, Cho JS (2021) Rational design of perforated bimetallic (Ni, Mo) sulfides/N-doped graphitic carbon composite microspheres as anode materials for superior Na-ion batteries. Small Methods 5(9):2100195. https://doi.org/10.1002/smtd.202100195
60. Kim CS, Saroha R, Choi HH, Oh JH, Park GD, Kang D-W, Cho JS (2023) High-performance cathode promoted by reduced graphene oxide nanofibers with well-defined interconnected meso-/micro pores for rechargeable Li-Se batteries. J Ind Eng Chem 121(1):489–498. https://doi.org/10.1016/j.jiec.2023.02.004
61. Xie P, Zhang Z, Liu K, Qian L, Dang F, Liu Y, Fan R, Wang X, Dou S (2017) C/SiO_2 meta-composite: overcoming the λ/a relationship limitation in metamaterials. Carbon 125(1):1–8. https://doi.org/10.1016/j.carbon.2017.09.021
62. Hao Y, Leng Z, Yu C, Xie P, Meng S, Zhou L, Li Y, Liang G, Li X, Liu C (2023) Ultra-lightweight hollow bowl-like carbon as microwave absorber owning broad band and low filler loading. Carbon 212(1):118156. https://doi.org/10.1016/j.carbon.2023.118156
63. Xie P, Li H, He B, Dang F, Lin J, Fan R, Hou C, Liu H, Zhang J, Ma Y (2018) Bio-gel derived nickel/carbon nanocomposites with

enhanced microwave absorption. J Mater Chem C 6(32):8812–8822. https://doi.org/10.1039/C8TC02127A
64. Kim CS, Lee JS, Saroha R, Park YB, Kang YC, Kang D-W, Jeong SM, Cho JS (2022) Porous nitrogen-doped graphene nanofibers comprising metal organic framework-derived hollow and ultrafine layered double metal oxide nanocrystals as high-performance anodes for lithium-ion batteries. J Power Sources 523(1):231030. https://doi.org/10.1016/j.jpowsour.2022.231030
65. Lee JS, Saroha R, Oh JH, Cho C, Jin B, Kang D-W, Cho JS (2022) Camphene-derived hollow and porous nanofibers decorated with hollow NiO nanospheres and graphitic carbon as anodes for efficient lithium-ion storage. J Ind Eng Chem 114(1):276–287. https://doi.org/10.1016/j.jiec.2022.07.017
66. Lee JS, Ka HS, Saroha R, Kang YC, Kang D-W, Cho JS (2023) Three-dimensional hierarchically porous micro sponge-ball comprising anatase TiO_2 nanodots and nitrogen-doped graphitic carbon as anodes for ultra-stable lithium-ion batteries. J Energy Storage 66(1):107396. https://doi.org/10.1016/j.est.2023.107396
67. Oh SH, Park SM, Kang D-W, Kang YC, Cho JS (2020) Fibrous network of highly integrated carbon nanotubes/MoO_3 composite bundles anchored with MoO_3 nanoplates for superior lithium ion battery anodes. J Ind Eng Chem 83(1):438–448. https://doi.org/10.1016/j.jiec.2019.12.017
68. Saroha R, Choi HH, Cho JS (2023) Boosting redox kinetics using rationally engineered cathodic interlayers comprising porous rGO–CNT framework microspheres with $NiSe_2$-core@N-doped graphitic carbon shell nanocrystals for stable Li–S batteries. Chem Eng J 473:145391. https://doi.org/10.1016/j.cej.2023.145391
69. Kim CS, Saroha R, Cho JS (2023) N-doped graphene nanofibers with porous channel comprising FeS nanocrystals and intertwined N-doped CNTs as efficient interlayers for Li-S batteries. Int J Energy Res 2023:3610577. https://doi.org/10.1155/2023/3610577
70. Chung S-H, Luo L, Manthiram A (2018) TiS_2–Polysulfide hybrid cathode with high sulfur loading and low electrolyte consumption for lithium–sulfur batteries. ACS Energy Lett 3(3):568–573. https://doi.org/10.1021/acsenergylett.7b01321

Publisher's Note Springer Nature remains neutral with regard to jurisdictional claims in published maps and institutional affiliations.

Springer Nature or its licensor (e.g. a society or other partner) holds exclusive rights to this article under a publishing agreement with the author(s) or other rightsholder(s); author self-archiving of the accepted manuscript version of this article is solely governed by the terms of such publishing agreement and applicable law.